Euclid: From Galaxies to Gravitational Waves – Forecasting Stochastic Gravitational Wave Background Anisotropies and Their Cross-Correlation[a]

K. Z. Yang,[1,†] G. Cusin,[2,3] V. Mandic,[1] C. Scarlata,[1,‡] J. Suresh,[4] B. Altieri,[5] N. Auricchio,[6] C. Baccigalupi,[7,8,9,10] M. Baldi,[11,6,12] S. Bardelli,[6] A. Biviano,[8,7] E. Branchini,[13,14,15] M. Brescia,[16,17] S. Camera,[18,19,20] G. Cañas-Herrera,[21,22] V. Capobianco,[20] C. Carbone,[23] J. Carretero,[24,25] S. Casas,[26,27] M. Castellano,[28] G. Castignani,[6] S. Cavuoti,[17,29] K. C. Chambers,[30] A. Cimatti,[31] C. Colodro-Conde,[32] G. Congedo,[33] L. Conversi,[34,5] Y. Copin,[35] A. Costille,[36] F. Courbin,[37,38,39] H. M. Courtois,[40] H. Degaudenzi,[41] G. De Lucia,[8] H. Dole,[42] F. Dubath,[41] X. Dupac,[5] S. Dusini,[43] S. Escoffier,[44] M. Farina,[45] R. Farinelli,[6] F. Faustini,[28,46] S. Ferriol,[35] F. Finelli,[6,47] P. Fosalba,[48,49] N. Fourmanoit,[44] M. Frailis,[8] E. Franceschi,[6] M. Fumana,[23] S. Galeotta,[8] K. George,[50] B. Gillis,[33] C. Giocoli,[6,12] P. Gómez-Alvarez,[51,5] J. Gracia-Carpio,[52] A. Grazian,[53] F. Grupp,[52,54] S. V. H. Haugan,[55] W. Holmes,[56] F. Hormuth,[57] A. Hornstrup,[58,59] K. Jahnke,[60] M. Jhabvala,[61] B. Joachimi,[62] E. Keihänen,[63] S. Kermiche,[44] A. Kiessling,[56] B. Kubik,[35] M. Kunz,[64] H. Kurki-Suonio,[65,66] A. M. C. Le Brun,[67] S. Ligori,[20] P. B. Lilje,[55] V. Lindholm,[65,66] I. Lloro,[68] G. Mainetti,[69] D. Maino,[70,23,71] O. Mansutti,[8] S. Marcin,[72] O. Marggraf,[73] M. Martinelli,[28,74] N. Martinet,[36] F. Marulli,[75,6,12] E. Medinaceli,[6] S. Mei,[76,77] Y. Mellier,[78,2] M. Meneghetti,[6,12] E. Merlin,[28] G. Meylan,[79] A. Mora,[80] M. Moresco,[75,6] L. Moscardini,[75,6,12] C. Neissner,[81,25] S.-M. Niemi,[21] C. Padilla,[81] S. Paltani,[41] F. Pasian,[8] K. Pedersen,[82] V. Pettorino,[21] S. Pires,[83] G. Polenta,[46] M. Poncet,[84] L. A. Popa,[85] L. Pozzetti,[6] F. Raison,[52] A. Renzi,[86,43] J. Rhodes,[56] G. Riccio,[17] E. Romelli,[8] M. Roncarelli,[6] R. Saglia,[54,52] Z. Sakr,[87,88,89] D. Sapone,[90] B. Sartoris,[54,8] M. Schirmer,[60] P. Schneider,[73] A. Secroun,[44] E. Sefusatti,[8,7,9] G. Seidel,[60] S. Serrano,[48,91,49] C. Sirignano,[86,43] G. Sirri,[12] L. Stanco,[43] J. Steinwagner,[52] P. Tallada-Crespí,[24,25] A. N. Taylor,[33] I. Tereno,[92,93] N. Tessore,[94] S. Toft,[95,96] R. Toledo-Moreo,[97] F. Torradeflot,[25,24] I. Tutusaus,[49,48,88] L. Valenziano,[6,47] J. Valiviita,[65,66] T. Vassallo,[8] A. Veropalumbo,[15,14,13] J. Weller,[54,52] G. Zamorani,[6] F. M. Zerbi,[15] E. Zucca,[6] T. Castro,[8,9,7,98] J. García-Bellido,[99] V. Scottez,[78,100] M. Viel,[7,8,10,9,98] and P. Monaco[101,8,9,7]

[1]*Minnesota Institute for Astrophysics, University of Minnesota, 116 Church St SE, Minneapolis, MN 55455, USA*
[2]*Institut d'Astrophysique de Paris, UMR 7095, CNRS, and Sorbonne Université, 98 bis boulevard Arago, 75014 Paris, France*
[3]*Departement of Theoretical Physics, University of Geneva, Switzerland*
[4]*Université Côte d'Azur, Observatoire de la Côte d'Azur, CNRS, Artemis, F-06304 Nice, France*
[5]*ESAC/ESA, Camino Bajo del Castillo, s/n., Urb. Villafranca del Castillo, 28692 Villanueva de la Cañada, Madrid, Spain*
[6]*INAF-Osservatorio di Astrofisica e Scienza dello Spazio di Bologna, Via Piero Gobetti 93/3, 40129 Bologna, Italy*
[7]*IFPU, Institute for Fundamental Physics of the Universe, via Beirut 2, 34151 Trieste, Italy*
[8]*INAF-Osservatorio Astronomico di Trieste, Via G. B. Tiepolo 11, 34143 Trieste, Italy*
[9]*INFN, Sezione di Trieste, Via Valerio 2, 34127 Trieste TS, Italy*
[10]*SISSA, International School for Advanced Studies, Via Bonomea 265, 34136 Trieste TS, Italy*

[a]This paper is published on behalf of the Euclid Consortium.

[11]*Dipartimento di Fisica e Astronomia, Università di Bologna, Via Gobetti 93/2, 40129 Bologna, Italy*
[12]*INFN-Sezione di Bologna, Viale Berti Pichat 6/2, 40127 Bologna, Italy*
[13]*Dipartimento di Fisica, Università di Genova, Via Dodecaneso 33, 16146, Genova, Italy*
[14]*INFN-Sezione di Genova, Via Dodecaneso 33, 16146, Genova, Italy*
[15]*INAF-Osservatorio Astronomico di Brera, Via Brera 28, 20122 Milano, Italy*
[16]*Department of Physics "E. Pancini", University Federico II, Via Cinthia 6, 80126, Napoli, Italy*
[17]*INAF-Osservatorio Astronomico di Capodimonte, Via Moiariello 16, 80131 Napoli, Italy*
[18]*Dipartimento di Fisica, Università degli Studi di Torino, Via P. Giuria 1, 10125 Torino, Italy*
[19]*INFN-Sezione di Torino, Via P. Giuria 1, 10125 Torino, Italy*
[20]*INAF-Osservatorio Astrofisico di Torino, Via Osservatorio 20, 10025 Pino Torinese (TO), Italy*
[21]*European Space Agency/ESTEC, Keplerlaan 1, 2201 AZ Noordwijk, The Netherlands*
[22]*Leiden Observatory, Leiden University, Einsteinweg 55, 2333 CC Leiden, The Netherlands*
[23]*INAF-IASF Milano, Via Alfonso Corti 12, 20133 Milano, Italy*
[24]*Centro de Investigaciones Energéticas, Medioambientales y Tecnológicas (CIEMAT), Avenida Complutense 40, 28040 Madrid, Spain*
[25]*Port d'Informació Científica, Campus UAB, C. Albareda s/n, 08193 Bellaterra (Barcelona), Spain*
[26]*Institute for Theoretical Particle Physics and Cosmology (TTK), RWTH Aachen University, 52056 Aachen, Germany*
[27]*Deutsches Zentrum für Luft- und Raumfahrt e. V. (DLR), Linder Höhe, 51147 Köln, Germany*
[28]*INAF-Osservatorio Astronomico di Roma, Via Frascati 33, 00078 Monteporzio Catone, Italy*
[29]*INFN section of Naples, Via Cinthia 6, 80126, Napoli, Italy*
[30]*Institute for Astronomy, University of Hawaii, 2680 Woodlawn Drive, Honolulu, HI 96822, USA*
[31]*Dipartimento di Fisica e Astronomia "Augusto Righi" - Alma Mater Studiorum Università di Bologna, Viale Berti Pichat 6/2, 40127 Bologna, Italy*
[32]*Instituto de Astrofísica de Canarias, E-38205 La Laguna, Tenerife, Spain*
[33]*Institute for Astronomy, University of Edinburgh, Royal Observatory, Blackford Hill, Edinburgh EH9 3HJ, UK*
[34]*European Space Agency/ESRIN, Largo Galileo Galilei 1, 00044 Frascati, Roma, Italy*
[35]*Université Claude Bernard Lyon 1, CNRS/IN2P3, IP2I Lyon, UMR 5822, Villeurbanne, F-69100, France*
[36]*Aix-Marseille Université, CNRS, CNES, LAM, Marseille, France*
[37]*Institut de Ciències del Cosmos (ICCUB), Universitat de Barcelona (IEEC-UB), Martí i Franquès 1, 08028 Barcelona, Spain*
[38]*Institució Catalana de Recerca i Estudis Avançats (ICREA), Passeig de Lluís Companys 23, 08010 Barcelona, Spain*
[39]*Institut de Ciencies de l'Espai (IEEC-CSIC), Campus UAB, Carrer de Can Magrans, s/n Cerdanyola del Vallés, 08193 Barcelona, Spain*
[40]*UCB Lyon 1, CNRS/IN2P3, IUF, IP2I Lyon, 4 rue Enrico Fermi, 69622 Villeurbanne, France*
[41]*Department of Astronomy, University of Geneva, ch. d'Ecogia 16, 1290 Versoix, Switzerland*

[42]*Université Paris-Saclay, CNRS, Institut d'astrophysique spatiale, 91405, Orsay, France*
[43]*INFN-Padova, Via Marzolo 8, 35131 Padova, Italy*
[44]*Aix-Marseille Université, CNRS/IN2P3, CPPM, Marseille, France*
[45]*INAF-Istituto di Astrofisica e Planetologia Spaziali, via del Fosso del Cavaliere, 100, 00100 Roma, Italy*
[46]*Space Science Data Center, Italian Space Agency, via del Politecnico snc, 00133 Roma, Italy*
[47]*INFN-Bologna, Via Irnerio 46, 40126 Bologna, Italy*
[48]*Institut d'Estudis Espacials de Catalunya (IEEC), Edifici RDIT, Campus UPC, 08860 Castelldefels, Barcelona, Spain*
[49]*Institute of Space Sciences (ICE, CSIC), Campus UAB, Carrer de Can Magrans, s/n, 08193 Barcelona, Spain*
[50]*University Observatory, LMU Faculty of Physics, Scheinerstr. 1, 81679 Munich, Germany*
[51]*FRACTAL S.L.N.E., calle Tulipán 2, Portal 13 1A, 28231, Las Rozas de Madrid, Spain*
[52]*Max Planck Institute for Extraterrestrial Physics, Giessenbachstr. 1, 85748 Garching, Germany*
[53]*INAF-Osservatorio Astronomico di Padova, Via dell'Osservatorio 5, 35122 Padova, Italy*
[54]*Universitäts-Sternwarte München, Fakultät für Physik, Ludwig-Maximilians-Universität München, Scheinerstr. 1, 81679 München, Germany*
[55]*Institute of Theoretical Astrophysics, University of Oslo, P.O. Box 1029 Blindern, 0315 Oslo, Norway*
[56]*Jet Propulsion Laboratory, California Institute of Technology, 4800 Oak Grove Drive, Pasadena, CA, 91109, USA*
[57]*Felix Hormuth Engineering, Goethestr. 17, 69181 Leimen, Germany*
[58]*Technical University of Denmark, Elektrovej 327, 2800 Kgs. Lyngby, Denmark*
[59]*Cosmic Dawn Center (DAWN), Denmark*
[60]*Max-Planck-Institut für Astronomie, Königstuhl 17, 69117 Heidelberg, Germany*
[61]*NASA Goddard Space Flight Center, Greenbelt, MD 20771, USA*
[62]*Department of Physics and Astronomy, University College London, Gower Street, London WC1E 6BT, UK*
[63]*Department of Physics and Helsinki Institute of Physics, Gustaf Hällströmin katu 2, University of Helsinki, 00014 Helsinki, Finland*
[64]*Université de Genève, Département de Physique Théorique and Centre for Astroparticle Physics, 24 quai Ernest-Ansermet, CH-1211 Genève 4, Switzerland*
[65]*Department of Physics, P.O. Box 64, University of Helsinki, 00014 Helsinki, Finland*
[66]*Helsinki Institute of Physics, Gustaf Hällströmin katu 2, University of Helsinki, 00014 Helsinki, Finland*
[67]*Laboratoire d'etude de l'Univers et des phenomenes eXtremes, Observatoire de Paris, Université PSL, Sorbonne Université, CNRS, 92190 Meudon, France*
[68]*SKAO, Jodrell Bank, Lower Withington, Macclesfield SK11 9FT, UK*
[69]*Centre de Calcul de l'IN2P3/CNRS, 21 avenue Pierre de Coubertin 69627 Villeurbanne Cedex, France*
[70]*Dipartimento di Fisica "Aldo Pontremoli", Università degli Studi di Milano, Via Celoria 16, 20133 Milano, Italy*
[71]*, Dipartimento di Fisica "Aldo Pontremoli", Università degli Studi di Milano, Via Celoria 16, 20133 Milano, Italy*

[72]*University of Applied Sciences and Arts of Northwestern Switzerland, School of Computer Science, 5210 Windisch, Switzerland*
[73]*Universität Bonn, Argelander-Institut für Astronomie, Auf dem Hügel 71, 53121 Bonn, Germany*
[74]*INFN-Sezione di Roma, Piazzale Aldo Moro, 2 - c/o Dipartimento di Fisica, Edificio G. Marconi, 00185 Roma, Italy*
[75]*Dipartimento di Fisica e Astronomia "Augusto Righi" - Alma Mater Studiorum Università di Bologna, via Piero Gobetti 93/2, 40129 Bologna, Italy*
[76]*Université Paris Cité, CNRS, Astroparticule et Cosmologie, 75013 Paris, France*
[77]*CNRS-UCB International Research Laboratory, Centre Pierre Binétruy, IRL2007, CPB-IN2P3, Berkeley, USA*
[78]*Institut d'Astrophysique de Paris, 98bis Boulevard Arago, 75014, Paris, France*
[79]*Institute of Physics, Laboratory of Astrophysics, Ecole Polytechnique Fédérale de Lausanne (EPFL), Observatoire de Sauverny, 1290 Versoix, Switzerland*
[80]*Telespazio UK S.L. for European Space Agency (ESA), Camino bajo del Castillo, s/n, Urbanizacion Villafranca del Castillo, Villanueva de la Cañada, 28692 Madrid, Spain*
[81]*Institut de Física d'Altes Energies (IFAE), The Barcelona Institute of Science and Technology, Campus UAB, 08193 Bellaterra (Barcelona), Spain*
[82]*DARK, Niels Bohr Institute, University of Copenhagen, Jagtvej 155, 2200 Copenhagen, Denmark*
[83]*Université Paris-Saclay, Université Paris Cité, CEA, CNRS, AIM, 91191, Gif-sur-Yvette, France*
[84]*Centre National d'Etudes Spatiales – Centre spatial de Toulouse, 18 avenue Edouard Belin, 31401 Toulouse Cedex 9, France*
[85]*Institute of Space Science, Str. Atomistilor, nr. 409 Măgurele, Ilfov, 077125, Romania*
[86]*Dipartimento di Fisica e Astronomia "G. Galilei", Università di Padova, Via Marzolo 8, 35131 Padova, Italy*
[87]*Institut für Theoretische Physik, University of Heidelberg, Philosophenweg 16, 69120 Heidelberg, Germany*
[88]*Institut de Recherche en Astrophysique et Planétologie (IRAP), Université de Toulouse, CNRS, UPS, CNES, 14 Av. Edouard Belin, 31400 Toulouse, France*
[89]*Université St Joseph; Faculty of Sciences, Beirut, Lebanon*
[90]*Departamento de Física, FCFM, Universidad de Chile, Blanco Encalada 2008, Santiago, Chile*
[91]*Satlantis, University Science Park, Sede Bld 48940, Leioa-Bilbao, Spain*
[92]*Departamento de Física, Faculdade de Ciências, Universidade de Lisboa, Edifício C8, Campo Grande, PT1749-016 Lisboa, Portugal*
[93]*Instituto de Astrofísica e Ciências do Espaço, Faculdade de Ciências, Universidade de Lisboa, Tapada da Ajuda, 1349-018 Lisboa, Portugal*
[94]*Mullard Space Science Laboratory, University College London, Holmbury St Mary, Dorking, Surrey RH5 6NT, UK*

[95]*Cosmic Dawn Center (DAWN)*
[96]*Niels Bohr Institute, University of Copenhagen, Jagtvej 128, 2200 Copenhagen, Denmark*
[97]*Universidad Politécnica de Cartagena, Departamento de Electrónica y Tecnología de Computadoras, Plaza del Hospital 1, 30202 Cartagena, Spain*
[98]*ICSC - Centro Nazionale di Ricerca in High Performance Computing, Big Data e Quantum Computing, Via Magnanelli 2, Bologna, Italy*
[99]*Instituto de Física Teórica UAM-CSIC, Campus de Cantoblanco, 28049 Madrid, Spain*
[100]*ICL, Junia, Université Catholique de Lille, LITL, 59000 Lille, France*
[101]*Dipartimento di Fisica - Sezione di Astronomia, Università di Trieste, Via Tiepolo 11, 34131 Trieste, Italy*

We estimate the amplitude and spatial anisotropy in the stochastic gravitational wave background (SGWB) energy density due to compact binary coalescence (CBC) events: binary black holes (BBH), binary neutron stars (BNS), and black hole-neutron star (BHNS) mergers. Our starting point is the Flagship Simulation Galaxy Catalogue developed by the Euclid Consortium. For each galaxy in the Catalogue, we use the simulated mass and star-formation to constrain the galaxy's star-formation history, and predict its contribution to the gravitational-wave energy density through CBC mergers. Combining such contributions from all galaxies in the Catalogue results in a prediction for the frequency spectrum and spatial anisotropy of the CBC SGWB. We also compare this prediction to semi-analytical models of SGWB generated by compact binaries. We identify a set of effective parameters that capture the key features of these models, and we apply a Bayesian framework to infer these parameters assuming an ideal scenario of cosmic variance-limited search. This represents the first step toward developing a comprehensive framework that will eventually enable the correlation of SGWB anisotropy and *Euclid* galaxy data, potentially allowing us to extract valuable astrophysical information from this new observable.

I. INTRODUCTION

Terrestrial gravitational wave (GW) detectors Advanced LIGO [1], Advanced Virgo [2], and KAGRA [3] have observed over two hundred signals from compact binary mergers [4] to date, including binary black holes (BBH), binary neutron stars (BNS), and neutron star-black hole (NSBH) systems. These observations have enabled measurements of rates and distributions of binary systems [5], tests of General Relativity [6], independent measurements of the Hubble constant [7], and examinations of the neutron star equation of state [8], among others.

One of the most compelling targets for the future observing runs of terrestrial GW detectors is the stochastic gravitational-wave background (SGWB), the superposition of many uncorrelated signals [9, 10]. Because SGWB inherits anisotropies from the large-scale distribution of its sources, cross-correlating SGWB anisotropies with maps of galaxy number counts is crucial for extracting astrophysical and cosmological information and for mitigating Poisson shot noise

† yang5991@umn.edu
‡

[11–22] (see also [23, 24] for recent Pulsar Timing Arrays experiments). In this work, we highlight the complementarity between SGWB and galaxy maps by leveraging the *Euclid* Flagship Simulation Galaxy Catalogue [25], to predict both the SGWB angular power spectrum and its cross-correlation with the galaxy distribution, and by identifying the key astrophysical parameters that these joint measurements can constrain. The full impact of *Euclid* observational systematics will be addressed in a future work.

The *Euclid* Wide Survey (EWS) will deliver quasi–full-sky coverage ($\sim 14\,000\,\mathrm{deg}^2$ of low-extinction extragalactic sky) with uniform, space-based optical+NIR imaging and slitless NIR spectroscopy. This combination provides exactly the ingredients required to cross-correlate SGWB anisotropies with galaxy maps: *i*) Very wide angular coverage, enabling robust recovery of the lowest multipoles well matching the expected resolution of the SGWB; *ii*) high galaxy number density with tomographic photo-z bins for shot-noise suppression and redshift localization of the cross-correlation signal; and *iii*) stable, homogeneous systematics control (PSF, depth, completeness, stellar contamination, and dust extinction) across a contiguous footprint that overlaps the terrestrial GW network. Taken together, these properties make the EWS not merely suitable but eventually the ideal, and possibly unique, dataset for a mature SGWB-galaxy cross-correlation measurement, combining near–all-sky angular reach with the depth, number density, and calibration fidelity needed to turn a detection into precise astrophysical and cosmological inference.

The SGWB is expected to include contributions from a wide array of early-Universe processes, primordial tensor fluctuations [26–29], inflation with gauge-field backreaction [30, 31], post-inflationary parametric resonance [32], and cosmic (super)strings [33–36], as well as from numerous astrophysical sources such as compact binary coalescences (BBH, BNS, NSBH) [37–39], rotating neutron stars [40–42], and supernovae [10, 43]. While cosmological components are typically stationary and continuous over observation time, the astrophysical background in the frequency band of ground-based detectors is "popcorn-like," reflecting the discrete and short-lived nature of mergers in band. Consequently, the SGWB angular power spectrum from compact binaries contains a prominent Poisson shot-noise term in addition to clustering [11–14]. Cross-correlating a shot-noise–dominated SGWB map with a dense galaxy map has been shown to alleviate shot-noise limitations, enabling sharper inference from Earth-based GW detectors [11–19].

To model SGWB anisotropies induced by large-scale distribution of astrophysical sources, one may adopt semi-analytic prescriptions for the galaxy distribution (e.g., [17, 44]) or populate large mock galaxy catalogues using recipes for compact-binary formation and merger rates [45]. In the latter approach, the growth of dark matter structure is first simulated and the history of the hierarchical mass assembly is then recorded by means of merger trees of haloes and subhaloes within snapshots stored at different time steps.

In this paper, we use the *Euclid* Flagship Simulation Galaxy Catalogue (version 2.1.10) [25] to sample the galaxy distribution. The Catalogue includes 4.8 billion galaxies across one octant of the sky and at redshifts up to 3. We implement a star-formation history (SFH) model $\psi(z)$ for each galaxy, driven by its current star-formation rate and total stellar mass specified in the Catalogue. We combine the SFH model with a distribution of time delay $p(t_\mathrm{d})$ between binary formation and merger and with the distribution of metallicity $p(\mathcal{Z})$ to obtain the merger rate of compact binaries hosted by the galaxies. We use the estimates of the mass distribution for compact binaries, provided by Advanced LIGO and Advanced Virgo observations through GWTC-3 [46], and follow the method of [45] to compute the SGWB energy density due to the entire population of merging compact binaries. We predict both the angular power spectrum of the resulting SGWB anisotropy and its cross-correlation with the galaxy distribution. These angular spectra, therefore, encode the relevant astrophysical information defined by the SFH ψ, delayed time distribution $p(t_\mathrm{d})$, and metallicity distribution $p(\mathcal{Z})$. In other words, the measurements of the SGWB angular power spectrum and the SGWB-galaxy correlation angular power spectrum can be used to constrain the combination of ψ, $p(t_\mathrm{d})$, and $p(\mathcal{Z})$. Combining these measurements with other observations (e.g. SFH ψ measurements by *Euclid*) can then further constrain the remaining quantities: $p(t_\mathrm{d})$ and $p(\mathcal{Z})$.

We also compare the angular spectra computed using the *Euclid* Flagship Simulation Galaxy Catalogue with the spectra predicted by semi-analytic astrophysical models, such as the ones explored in [14, 44]. We identify a set of effective parameters that capture the main features of the semi-analytic models, and we apply a Bayesian formalism to infer their values based on the comparisons of the models with the simulation based on the Catalogue. This approach enables us to identify the range of (effective) astrophysical parameters consistent with the predictions derived from the Catalogue. When applied to real data, this methodology will help determine which class of semi-analytic models and parameters best describe observations.

This paper is structured as follows. In Sect. II we present the astrophysical model of angular power spectra of SGWB fluctuations, galaxy over-density and their cross-correlations. In Sect. III we review the approach of [47] of populating a galaxy catalogue with compact binary mergers and predicting the corresponding SGWB spectrum. We present the properties of the *Euclid* Flagship Simulation Galaxy Catalogue in Sect. IV and the SGWB angular power spectra predicted by it in Sect. V. We conclude in Sect. VI.

II. MODELLING ANISOTROPIES AND CROSS-CORRELATIONS

The observed GW energy density parameter, Ω_GW is defined as the background energy density ρ_GW per units of logarithmic frequency f and solid angle $\mathbf{e} = (\theta, \phi)$, normalized by the critical density of the Universe today ρ_c and the speed of light c. It can be divided into an isotropic background contribution $\bar{\Omega}_\mathrm{GW}$ and a contribution from anisotropic perturbations $\delta\Omega_\mathrm{GW}$ [14, 48–51] as

$$\Omega_\mathrm{GW}(\mathbf{e}, f) = \frac{f}{\rho_\mathrm{c}\, c} \frac{\mathrm{d}^3\rho_\mathrm{GW}}{\mathrm{d}^2\mathbf{e}\,\mathrm{d}f}(\mathbf{e}, f) = \frac{\bar{\Omega}_\mathrm{GW}(f)}{4\pi} + \delta\Omega_\mathrm{GW}(\mathbf{e}, f)\,, \tag{II.1}$$

where the isotropic background spectrum can be written as the integral over conformal distance r

$$\bar{\Omega}_\mathrm{GW}(f) = \int \mathrm{d}r\, \partial_r\, \bar{\Omega}_\mathrm{GW}(f, r) = \int \mathrm{d}r\, \frac{f}{\rho_\mathrm{c}\, c}\, \mathcal{A}(f, r)\,. \tag{II.2}$$

The integral in Eq. (II.2) runs over an interval of time $[r_*, r_\mathrm{o}]$ where r_o is the conformal distance, and r_* is the maximal distance, which in our case, is chosen to be the distance at a maximum redshift $z = 7$. The function $\mathcal{A}(f, r)$ is an astrophysical kernel that contains information on the local production of GWs at galaxy scales. Schematically this kernel can be parameterized as [13]

$$\mathcal{A}(f, r) = \frac{a^4}{4\pi} \int \mathrm{d}\mathcal{L}_\mathrm{GW}\, \bar{n}_\mathrm{G}(\mathcal{L}_\mathrm{GW}, r)\, \mathcal{L}_\mathrm{GW}\,, \tag{II.3}$$

where a is the scale factor of the Universe and $\bar{n}_\mathrm{G}$ is the average physical number density of galaxies at distance r with gravitational wave luminosity $\mathcal{L}_\mathrm{GW}$. Different astrophysical models give quite different predictions for this kernel, see e.g. [14] for an explorative approach. For the SGWB due to mergers of compact objects such as BBH and BNS, the low-frequency band ($f \lesssim 100$ Hz) is dominated by the inspiral phase contributions and follows a simple power law $\Omega_{\rm GW} \sim f^{2/3}$. The redshift dependence of the astrophysical kernel can be parameterized as a Gaussian distribution with parameters θ, which will be discussed in Section V C.

Since $\delta\Omega_{\rm GW}$ is a stochastic quantity, it can correlate with other cosmological stochastic observables. An interesting observable to look at is the cross-correlation of the SGWB with the distribution of galaxies, for example, with the galaxy number counts Δ defined as the overdensity of the number of galaxies per unit of redshift and solid angle

$$\Delta(\mathbf{e}, z) \equiv \frac{N(z, \mathbf{e}) - \bar{N}(z)}{\bar{N}(z)}\,, \tag{II.4}$$

where $\bar{N}(z)$ is the average galaxy number density at redshift z.

If astrophysical GW sources are located in galaxies, we would expect the SGWB and the galaxy distribution to have a high correlation level. The angular power spectrum of the GW and galaxy counts cross-correlations is defined as

$$C_\ell^{\rm cross}(f;\theta) \equiv \frac{1}{2\ell+1}\sum_{m=-\ell}^{\ell}\langle a_{\ell m}(f;\theta)\, b^*_{\ell m}\rangle\,, \tag{II.5}$$

where the brackets denote an ensemble average while $a_{\ell m}(f)$ and $b_{\ell m}$ are the coefficients of the spherical harmonics decomposition of the SGWB energy density and galaxy number counts, respectively. Explicitly

$$\delta\Omega_{\rm GW}(\mathbf{e}, f;\theta) = \sum_{\ell=0}^{\infty}\sum_{m=-\ell}^{\ell} a_{\ell m}(f;\theta)\, Y_{\ell m}(\mathbf{e})\,, \tag{II.6}$$

$$\Delta(\mathbf{e}) = \sum_{\ell=0}^{\infty}\sum_{m=-\ell}^{\ell} b_{\ell m}\, Y_{\ell m}(\mathbf{e})\,. \tag{II.7}$$

It can be shown that the angular power spectra of the cross-correlation are given by [48]

$$C_\ell^{\rm cross}(f;\theta) = \frac{2}{\pi}\int {\rm d}k\, k^2\, \delta\Omega^*_{{\rm GW},\ell}(k, f;\theta)\,\Delta_\ell(k)\,, \tag{II.8}$$

where k is the wave number. Keeping only the leading-order contribution to the anisotropy given by clustering (neglecting line-of-sight effects), we have

$$\delta\Omega_{{\rm GW},\ell}(k, f;\theta) = \frac{f}{4\pi\rho_{\rm c}\, c}\int {\rm d}r\, \mathcal{A}(r, f;\theta)\left[b(r)\,\delta_{{\rm m},k}(r)\, j_\ell(kr)\right], \tag{II.9}$$

$$\Delta_\ell(k) = \int {\rm d}r\, W(r)\left[b(r)\,\delta_{{\rm m},k}(r)\, j_\ell(kr)\right], \tag{II.10}$$

where j_ℓ are spherical Bessel functions, while $\delta_{\rm m}$ is the dark-matter over-density, related to galaxy overdensity via the bias factor b, which we assume to be scale-independent with redshift evolution given by $b(z) = b_0\sqrt{1+z}$ [52, 53] and $b_0 = 1.5$ [14], where this value has been set considering the measurement from the SDSS survey at $z = 0.6$. $W(r)$ is a window function normalized to one, which we choose to be flat, so it is equivalent to a cut of the observational redshift limit, in our case at $z = 3$.

III. METHOD REVIEW: PREDICTING CBCS FROM A CATALOGUE

We aim now to compute the background energy density due to GW emissions by compact binary coalescences (CBCs) scattered across galaxies in a galaxy catalogue. Following the method presented in section IV of [47], we calculate the energy density by summing up contributions from each galaxy, using

$$\Omega_{\rm GW}(\mathbf{e}, f) = \sum_k w_k(f)\, \delta_{\rm D}^{(2)}(\mathbf{e}, \mathbf{e}_k)\,, \tag{III.1}$$

where $\delta_{\rm D}^{(2)}(\mathbf{e}, \mathbf{e}_k) = \delta_{\rm D}(\cos\theta - \cos\theta_k)\, \delta_{\rm D}(\phi - \phi_k)$ is a 2-dimensional Dirac delta for the direction in the sky. The contribution from each galaxy is given by

$$w_k(f) \equiv \sum_i \frac{\pi H_0}{3}\, (t_H\, f_{\rm o})^3\, \frac{1+z_k}{r^2(z_k)}\, (1 + \mathbf{e}_k \cdot \boldsymbol{v}_{\rm o}) \int {\rm d}\zeta_{\rm b}\, R_i(z_k, \mathcal{Z}_k, \zeta_{\rm b})\, \mathcal{S}_i(f_{{\rm s},k}, \zeta_{\rm b})\,. \tag{III.2}$$

In this equation, R_i denotes the merger rate and $\mathcal{S}_i$ the source function, whose physical interpretation will be discussed below, and $t_H \equiv 1/H_0$ stands for the Hubble time. The index $i \in$ {BNS, BBH, BHNS} runs over the different types of binary mergers: binary neutron star systems, binary black hole systems, and black hole-neutron star systems. These binaries are described by parameters $\zeta_{\rm b}$, which we will assume to include the component masses $m_{1,2}$ and their spins $\chi_{1,2}$. Furthermore, $k \in \{1, 2, ..., \mathcal{N}\}$ indexes a sum over the galaxies in the catalogue, with each galaxy k described by its redshift z_k, comoving distance $r(z_k)$, sky location $\hat{\mathbf{e}}_k$, and log-normalized metallicity $\mathcal{Z}_k$ defined relative to the Solar metallicity $Z_\odot$

$$\mathcal{Z} \equiv \log_{10} \frac{Z}{Z_\odot}\,. \tag{III.3}$$

In Eq. (III.2), the source-frame GW frequency in galaxy k is related to the observed one via a redshift factor $f_{{\rm s},k} = f_{\rm o}\,(1 + z_k)$, where the subscript "s" represents "source-frame", and the observed redshift is related to the background one as $z_k = \bar{z}_x + \delta z$, where the perturbation δz accounts for all relativistic effects, and in particular for the effect due to the source and observer peculiar velocities, see [54] for a detailed discussion. Here we assume galaxy peculiar velocities to be negligible at high redshift, and we also neglect the observer velocity, setting $\boldsymbol{v}_{\rm o} \approx 0$. This corresponds to filtering out the contribution of a kinematic dipole from the source distribution function.

The source function $\mathcal{S}_i$ defines the GW energy spectrum emitted by a single binary, and it is a function of the source frame frequency $f_{{\rm s},k}$ and the binary parameters $\zeta_{\rm b}$. For BBH, it is given by

$$\mathcal{S}_{\rm BBH}(f_{\rm s}, \zeta_{\rm b}) = \frac{5 (G\, \mathcal{M})^{5/3}}{6\pi^{1/3}} \times \begin{cases} f_{\rm s}^{-7/3} \left[1 + \sum_{i=2}^{3} \alpha_i\, (\pi\, G\, M\, f_{\rm s})^{i/3}\right]^2, & f_{\rm s} < f_1 \\ c_1\, f_{\rm s}^{-4/3} \left[1 + \sum_{i=1}^{2} \epsilon_i\, (\pi\, G\, M\, f_{\rm s})^{i/3}\right]^2, & f_1 \le f_s < f_2 \\ c_2 \left[1 + \left(\frac{f_{\rm s} - f_2}{f_3}\right)\right]^2, & f_2 \le f_{\rm s} < f_4 \end{cases} \tag{III.4}$$

where definitions of $c_{1,2}, \alpha_i, \epsilon_i$ and $f_{1,2,3,4}$ can be found in [47, 55], and depend on the masses and spins of the binaries. Here, G is the Newton's gravitational constant, M stands for the total mass of the binary, and $\mathcal{M}$ stands for its chirp mass. For BNS and BHNS systems, only $f_{\rm s} < f_1$ terms will be kept, and contributions from higher frequencies can be ignored. The optimized inclination angle is assumed in this calculation.

The merger rate depicts the rate of the type i compact binary mergers in galaxy k and depends on the galaxy redshift, its metallicity, and the binary merger parameters

$$R_i(z_k, \mathcal{Z}_k, \zeta_{\rm b}) = \frac{\mathcal{R}_i^{\rm (local)}}{\mathcal{I}_i}\, p_i(\zeta_{\rm b})\, f_{\mathcal{Z}}\, \psi_{{\rm d},i}(z_k)\,. \tag{III.5}$$

Specifically, we assume the merger rate in a given galaxy will follow the rate ψ of star-formation in the galaxy, delayed by the lifetime of the binary between its formation and merger. To capture the variability in the time delay, we average over its probability distribution. Hence, the delayed star-formation rate is given by

$$\psi_{\mathrm{d},i}(z_k) = \frac{1}{\ln\left[t(z)/t_{\mathrm{min},i}\right]} \int_{t_{\mathrm{min},i}}^{t(z)} \mathrm{d}t_\mathrm{d}\, \frac{1}{t_\mathrm{d}}\, \psi[z_\mathrm{f}(z_k, t_\mathrm{d})]\,, \tag{III.6}$$

where the delay time t_d has a probability distribution $p(t_\mathrm{d}) \propto 1/t_\mathrm{d}$ between the minimum delay time $t_{\mathrm{min},i} = [20, 50, 50]$ Myr for $i = [\mathrm{BNS, BBH, BHNS}]$ and the maximum delay time t_max which is the age of the Universe $t(z)$. Here z_f is the formation redshift defined by the merger redshift z_k and the time delay t_d

$$1 + z_\mathrm{f}(z_k, t_\mathrm{d}) = (1 + z_k)\left[\cosh\left(\frac{3\Omega_\Lambda^{1/2}\, t_\mathrm{d}}{2t_H}\right) - \frac{E(z)}{\Omega_\Lambda^{1/2}}\, \sinh\left(\frac{3\Omega_\Lambda^{1/2}\, t_\mathrm{d}}{2t_H}\right)\right]^{-2/3}, \tag{III.7}$$

where $E(z) \equiv H(z)/H_0 = \sqrt{\Omega_\mathrm{m}(1+z)^3 + \Omega_\Lambda}$ assuming standard flat ΛCDM cosmology. The dependence of the merger rate on metallicity is captured by the correction factor $f_\mathcal{Z}$. Following [47], we assume that black holes with mass greater than $30M_\odot$ can only be formed in galaxies with relatively small metallicity: $Z \leq \frac{1}{2}Z_\odot$, or equivalently $\mathcal{Z} \leq \log_{10}\frac{1}{2} \approx -0.301 \equiv \mathcal{Z}_\mathrm{lim}$. Consequently,

$$f_\mathcal{Z}(\mathcal{Z}, m_1, m_2) = \begin{cases} 1, & m_1, m_2 < 30M_\odot\,, \\ \Theta(\mathcal{Z}_\mathrm{lim} - \mathcal{Z}), & \text{otherwise}\,. \end{cases} \tag{III.8}$$

The dependence on the binary merger parameters ζ_b is captured in the normalized probability distribution $p_i(\zeta_\mathrm{b})$. For simplicity, we set the neutron star spins to zero, and the masses uniformly distribute between $1.1M_\odot$ and $2.0M_\odot$; the black hole spins are set to be uniformly distributed between -1 and 1, with a mass distribution from the fiducial Power-law + Peak (PP) model in [46] (Fig. 10). The minimum and maximum masses of black holes are $M_\mathrm{BH}^\mathrm{min} = 5.08M_\odot$, $M_\mathrm{BH}^\mathrm{max} = 86.85M_\odot$. For BNS, both neutron stars follow the mass distribution and spin set above. For BHNS, the neutron star and the black hole follow the mass and spin distribution set above for them respectively. For BBH, the primary black hole follows the above mass and spin distribution, while the secondary black hole in the binary system has the same spin distribution but its mass is always smaller than that of the primary black hole.

Finally, we normalize the merger rate so that its local value (i.e. at $z = 0$) agrees with the fiducial model merger at redshift $z = 0$ with its lowest 5% and highest 95% confidence interval of GWTC-3 in [46]

$$\mathcal{R}_\mathrm{BBH}^\mathrm{(local)} = 23.9^{+14.9}_{-8.6}\ \mathrm{Gpc^{-3}\ yr^{-1}},\ \mathcal{R}_\mathrm{BNS}^\mathrm{(local)} = 105.5^{+190.2}_{-83.9}\ \mathrm{Gpc^{-3}\ yr^{-1}},\ \mathcal{R}_\mathrm{NSBH}^\mathrm{(local)} = 32.0^{+62.0}_{-24.0}\ \mathrm{Gpc^{-3}\ yr^{-1}}\,. \tag{III.9}$$

The BBH and BNS merger rates are in Sect. IV. A in [46], and the NSBH merger rate is chosen from the BGP model in Table II in [46]. As we do not know the distribution of the merger rate, we have to assume it is Gaussian, and the 68% confidence interval σ can be approximated as 1.6 times smaller than the 90% confidence interval in Eq. (III.9).

This requires the normalization factor $\mathcal{I}_i$ in Eq. (III.5), which is given by [47]

$$\mathcal{I}_i = \left\{\frac{1}{\ln\left[t(z)/t_{\mathrm{min},i}\right]} \int_{t_{\mathrm{min},i}}^{t(z)} \frac{\mathrm{d}t_\mathrm{d}}{t_\mathrm{d}}\, \psi^{(V)}(z_\mathrm{f})\, \frac{n(z)}{n(z_\mathrm{f})} \int \mathrm{d}\mathcal{Z}\, p(\mathcal{Z}|z) \int \mathrm{d}\zeta_\mathrm{b}\, p_i(\zeta_\mathrm{b})\, f_\mathcal{Z}\right\}\Bigg|_{z=0}\,, \tag{III.10}$$

where $\psi^{(V)}(z)$ is the sum of the galactic star-formation rates per unit comoving volume at redshift z, and $n(z)$ is the number of galaxies per comoving volume. $p(\mathcal{Z}|z)$ is the probability distribution of the log-normalized metallicity $\mathcal{Z}$ over redshift z. We will discuss how to estimate these three quantities using catalogue information and how to compute $\mathcal{I}_i$ in detail in Sect. IV.

Finally, to study anisotropy in this model, the SGWB energy density is expanded into spherical harmonics, with the coefficients given by

$$a_{\ell m}(f) \equiv \int_{S^2} d^2\sigma \, \Omega_{GW}(f, \mathbf{e}) \, Y^*_{\ell m}(\mathbf{e}) = \sum_k w_k(f) \, Y^*_{\ell m}(\mathbf{e}_k) \, . \tag{III.11}$$

IV. THE *EUCLID* FLAGSHIP SIMULATION: GALAXIES

Computing the SGWB with the method described above requires a simulated galaxy catalogue; we select the *Euclid* Flagship Simulation Galaxy Catalogue (v2.1.10) [25] hosted on CosmoHub [56, 57] because it is tailored to the properties of the *Euclid* Wide Survey (EWS), thereby positioning our pipeline to later propagate and quantify survey systematics directly on real *Euclid* data. This Catalogue is based on the record-setting Flagship2 N-body simulation that includes ∼4 trillion dark matter particles. It contains the properties of ∼4.8 billion galaxies up to $H_E < 26.6$ considering no selection of emission lines or corrections due to Milky Way extinction, distributed over one octant of the sky ($\sim$ 5157 deg^2) centered at approximately the North Galactic Pole ($145° < \mathrm{RA} < 235°, 0° < \mathrm{Dec} < 90°$), and in the redshift range between 0 and 3. Given that the SGWB includes signal from all galaxies, even those that are in principle not detectable, we include all simulated objects in the computation. The effects of observational selection functions in the estimate of the *Euclid* galaxy density and consequently in the measured cross-correlation, will be explored in a future paper.

For each galaxy, the Catalogue provides the following parameters needed in our calculation using the method in Sect. III: redshift z, star-formation rate ψ, stellar mass M_*, and metallicity $12 + \log_{10}(\mathrm{O/H})$. Following the galaxy metallicity distribution model in [58] that the *Euclid* Flagship Simulation Galaxy Catalogue [25] is using, the abundance of oxygen (O) relative to hydrogen (H) is defined as $12 + \log_{10}(\mathrm{O/H})$, and the Solar value is 8.69 [59]. The logarithmic normalized metallicity $\mathcal{Z}$ of galaxy is defined with respect to the Solar metallicity in Eq. (III.3), which is then related to the galaxy's $12 + \log_{10}(\mathrm{O/H})$ as

$$\mathcal{Z} \equiv \log_{10} \frac{Z}{Z_\odot} = \log_{10} \frac{[\mathrm{O/H}]}{[\mathrm{O/H}]_\odot} = \log_{10} \frac{10^{[12+\log_{10}(\mathrm{O/H})]-12}}{10^{8.69-12}} = [12 + \log_{10}(\mathrm{O/H})] - 8.69 \, . \tag{IV.1}$$

In order to compute the merger rate in Eq. (III.5), our model requires the galaxy's delayed star-formation rate ψ_d. This, in turn, requires a model of the galaxy SFH, which is not provided by the *Euclid* Flagship Simulation Galaxy Catalogue. We therefore impose an SFH model that leverages the information provided by the Catalogue: stellar mass M_* and star-formation rate $\psi(z_{obs})$ of the galaxy at its current redshift z_{obs}.

Following the literature on the topic [60–64], we implement a mixed model. Specifically, galaxies of stellar mass $M_* > 10^{10} M_\odot$ follow a log-normal exponential SFH model [65], given by

$$\psi(t) = \frac{A}{\sqrt{2\pi\tau^2}\, t} \exp\left\{ - \frac{\left[\ln\left(\frac{t}{1\,\mathrm{Gyr}}\right) - T_0\right]^2}{2\tau^2} \right\}, \tag{IV.2}$$

where A, T_0, τ are parameters, t is the time since the Big Bang. The cumulative SFH ψ_c, which is the integral of the SFR, gives the current stellar mass M_* of the galaxy at the time of observation

$$\psi_c(t) \equiv \int_0^t \mathrm{d}t'\ \psi(t') = \frac{A}{2}\left\{1 - \mathrm{erf}\left[-\frac{\ln\left(\frac{t}{1\,\mathrm{Gyr}}\right) - T_0}{\tau\sqrt{2}}\right]\right\}, \tag{IV.3}$$

$$\psi_c(t_{\rm obs}) = 10^9\, M_*\,. \tag{IV.4}$$

In order to constrain the three parameters A, T_0, τ with the two known quantities ψ, M_*, the power-law approximation of the relation between the size and centre of the $\psi - t$ curve peak is needed [65]

$$\sigma_{\rm peak} = 0.83\, t_{\rm peak}^{3/2}\,, \tag{IV.5}$$

These two peak parameters also depend on the three parameters mentioned above [65]

$$\frac{t_{\rm peak}}{1\,\mathrm{Gyr}} = \mathrm{e}^{T_0-\tau^2},\ \sigma_{\rm peak} = 2\,\frac{t_{\rm peak}}{1\,\mathrm{Gyr}}\ \sinh\left[\sqrt{2\ln(2)}\,\tau\right]. \tag{IV.6}$$

The power-law relation in Eq. (IV.5) is valid for a small portion of galaxies, so not all galaxies have numerical solutions using the log-normal exponential model. For those galaxies without valid solutions in this model, especially less massive galaxies, their $\sigma_{\rm peak}$ is large enough that it is reasonable to treat their SFH as flat

$$\psi(t) = \psi(t_{\rm obs}) \tag{IV.7}$$

between a start time t_0 and the time the galaxy is observed $t_{\rm obs}$. So the integral of the SFH gives the stellar mass M_*

$$\int_{t_0}^{t_{\rm obs}} \mathrm{d}t'\ \psi(t') = (t_{\rm obs} - t_0)\,\psi(t_{\rm obs}) = M_*\,, \tag{IV.8}$$

hence the start time $t_0 = t_{\rm obs} - M_*/\psi(t_{\rm obs})$.

The galaxy delayed star-formation rate is defined in Eq. (III.6). For some galaxies, the time since the first stars formed is shorter than 50 Myr, so they are not able to form BBH or BHNS ($\psi_{\rm d,BBH} = \psi_{\rm d,BHNS} = 0$). On the other hand, all *Euclid* Flagship Simulation Galaxy Catalogue galaxies have SFH longer than 20 Myr, so they are all able to form BNS. The median values with the 16th and 84th percentile of the distribution of $\psi_{{\rm d},i}$ for Catalogue galaxies in redshift bins of width 0.1 between 0 and 3 are shown in Fig. 1.

Further, the calculation of the merger rate in Eq. (III.5) also requires the normalization factor $\mathcal{I}_i$, which in turn relies on estimates of the redshift-dependent galaxy number density $n(z)$, the star-formation rate density $\psi^{(V)}(z)$, and the log-normalized metallicity probability distribution $p(\mathcal{Z}|z)$, as specified in Eq. (III.10). Recall from Eq. (III.8) that $f_{\mathcal{Z}}$ is a selection function such that only galaxies with $\mathcal{Z} \le \mathcal{Z}_{\rm lim}$ can produce black holes with mass $\ge 30M_\odot$. The last two integrals of $\mathcal{I}_i$ in Eq. (III.10) for i=BNS are unity; for i=BBH or BHNS, they can be written as

$$\int_{-\infty}^{\mathcal{Z}_{\rm max}} \mathrm{d}\mathcal{Z}\ p(\mathcal{Z}|z) \int \mathrm{d}\zeta_{\rm b}\ p_i(\zeta_{\rm b})\, f_{\mathcal{Z}} = \left[p\big(\mathcal{Z} < \mathcal{Z}_{\rm lim}|z\big)\int_{M_{\rm BH}^{\rm min}}^{M_{\rm BH}^{\rm max}} \mathrm{d}m_1 + p\big(\mathcal{Z} \ge \mathcal{Z}_{\rm lim}|z\big)\int_{M_{\rm BH}^{\rm min}}^{30M_\odot} \mathrm{d}m_1\right]$$
$$\times \begin{cases} \displaystyle\int_{M_{\rm BH}^{\rm min}}^{m_1} \mathrm{d}m_2 \int_{-1}^{1} \mathrm{d}\chi_1 \int_{-1}^{1} \mathrm{d}\chi_2\ p_i(\zeta_{\rm b})\,, & \text{BBH} \\ \displaystyle\int_{1.1M_\odot}^{2.0M_\odot} \mathrm{d}m_2 \int_{-1}^{1} \mathrm{d}\chi_1\ \delta(\chi_2)\, p_i(\zeta_{\rm b})\,, & \text{BHNS} \end{cases}. \tag{IV.9}$$

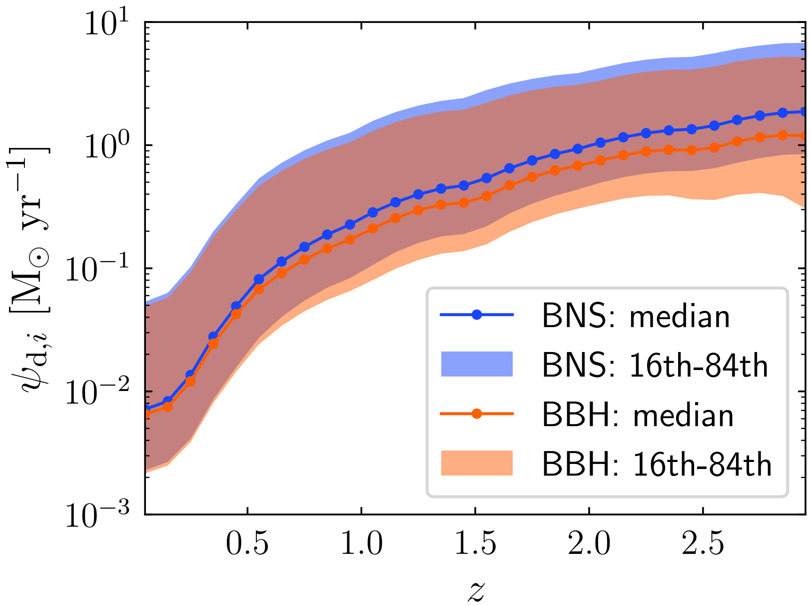

FIG. 1. The median, 16th and 84th percentile of the delayed star-formation rate computed for minimum time 20 and 50 Myr (corresponding to BNS and BBH or BHNS respectively) using the exponential-flat mixed SFH model for all *Euclid* Flagship Simulation Galaxy Catalogue galaxies with H_E less than 26.6 in redshift bins of 0.1 width.

Using information provided in the *Euclid* Flagship Simulation Galaxy Catalogue, we compute the three quantities $n(z)$, $\psi^{(V)}(z)$, and $p(\mathcal{Z} < \mathcal{Z}_\mathrm{lim}|z)$ in redshift bins of width 0.01[1]. We then use these distributions and a local estimation of $n(z = 0) \approx 0.223$ Mpc^{-3} to compute $\mathcal{I}_i$ in Eq. (III.10) for all types of binaries (BNS, BBH, BHNS).

Next, we note that there are three observational limitations of the *Euclid* Flagship Simulation Galaxy Catalogue. First, the Catalogue covers only $f_\mathrm{sky} = 1/8$ of the sky. This limit can be justified by evaluating all the galaxy densities properties (i.e., number density, star-formation rate density, etc.) within f_sky of the comoving volume and scaling up their density per comoving value by $1/f_\mathrm{sky}$. The angular power spectra C_ℓ should also scale up by $1/f_\mathrm{sky}$. This scaling is necessary for any galaxy catalogue that has partial-sky coverage.

Second, the Catalogue contains only galaxies with H_E less than 26.6. However, it also includes a 5×5 deg^2 deep region ($5^\circ < \mathrm{Dec} < 10^\circ, 150^\circ < \mathrm{RA} < 155^\circ$) that contains all galaxies with redshift between 0 and 3, and without any H_E magnitude constraint. This deep region indicates that a large portion (80%) of galaxies has H_E greater than or equal to 26.6. Nevertheless, due to their relatively large distance from Earth, these galaxies contribute little to the total GW energy density, less than 5%. Therefore, we ignore it for the rest of our calculation as it does not qualitatively impact our results. The distribution of galaxy number counts and GW energy density contributions as 2D histograms of H_E and redshift are shown in Fig. 2.

Third, the Catalogue contains only galaxies with a redshift smaller than 3. Under the assumption that most of the star-formation takes place at redshifts below 3 [64], combined with the stronger distance suppression of GW signals from higher redshifts, (cf. Eq. III.2), the SGWB energy density will be dominated by contributions from redshifts 2 and below. The redshift cutoff will, therefore, not have a qualitative impact on our results, and we demonstrate this in Sect. V A.

[1] Note that no observational effects specific to *Euclid* are included in this computation.

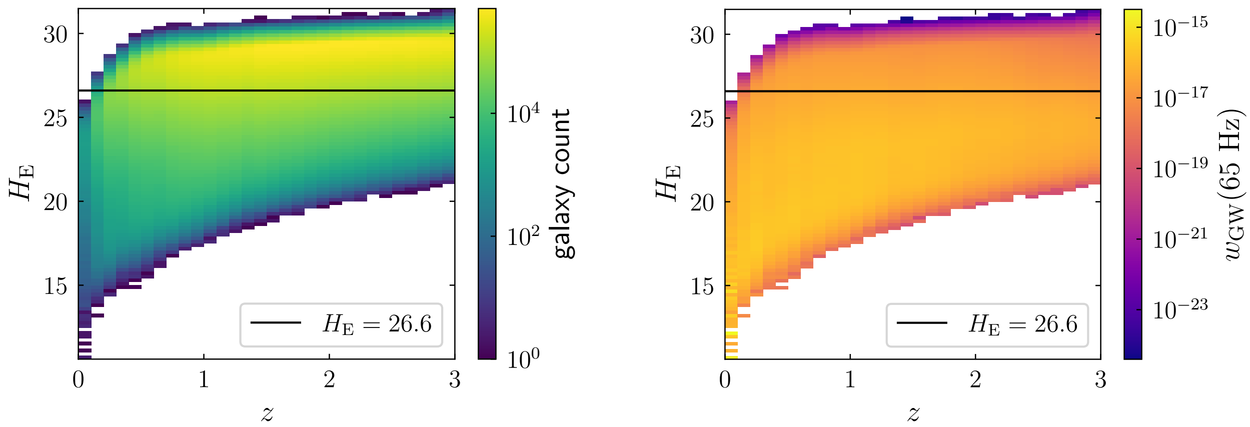

FIG. 2. 2D histogram of H_E and redshift with the colour bar being galaxy number count (*left*) or gravitational wave energy density (*right*) of all galaxies in *Euclid* deep region in $5^\circ < \mathrm{Dec} < 10^\circ, 150^\circ < \mathrm{RA} < 155^\circ$ with redshift up to 3. The black lines stand for $H_\mathrm{E} = 26.6$.

V. ESTIMATES OF THE GRAVITATIONAL-WAVE BACKGROUND AND ITS ANGULAR POWER SPECTRA

A. Total Gravitational-Wave Energy Density

Using data from the *Euclid* Flagship Simulation Galaxy Catalogue and following the procedure outlined in Sections III and IV, we compute the average expected GW energy density contribution w_k (cf. Eq. III.2) for every *Euclid* Flagship galaxy and for each of the three binary types: BBH, BNS, and BHNS. We emphasize that we include all galaxies from the Catalogue in this calculation, without including any observational effects specific to *Euclid*. Integrating over all of the galaxies in the Catalogue (and accounting for the factor of 8 due to the partial sky coverage) yields a prediction for the total GW energy density due to compact binary mergers.

Table I shows these predictions in comparison to the predictions of the semi-analytic model based on the latest version of the GW catalogue, GWTC-3 [46]. Our predictions for the energy density are about 10 times smaller than those of the semi-analytic model. We note that the semi-analytic model assumes the merger rate to follow the global star-formation rate in the Universe, convolved with the formation-to-merger time delay distribution. This is different from the galaxy-catalogue-based approach, which is limited to the galaxies available in the catalogue, and handles SFH separately for each individual galaxy.

The paper by Jenkins and others [47] has a calculation similar to the catalogue-based approach using the *Millennium* simulation. They do not give predictions of the total GW energy density, as they used a restricted sample of galaxies with $z < 0.78$. However, they give an analytical prediction that is 10 times bigger than the semi-analytic model. We note that this analytical calculation was based on earlier estimates of binary merger rates that were higher than those used both in this work and in the GWTC-3 estimate, being $\mathcal{R}^{(\mathrm{local})}_{\mathrm{BBH}} = 103^{+110}_{-63}\,\mathrm{Gpc}^{-3}\,\mathrm{yr}^{-1}$, $\mathcal{R}^{(\mathrm{local})}_{\mathrm{BNS}} = 1540^{+3200}_{-1220}\,\mathrm{Gpc}^{-3}\,\mathrm{yr}^{-1}$, $\mathcal{R}^{(\mathrm{local})}_{\mathrm{NSBH}} \leq 3600\,\mathrm{Gpc}^{-3}\,\mathrm{yr}^{-1}$, where the BBH and BNS rates are from implications of SGWB from the GW170817 event [66], and the BHNS rate is an upper limit from LIGO O1 [67]. As we continue to observe more GW transients through observing runs, the estimate of merger rates has improved.

Finally, we note that our predictions are consistent with the latest 95% confidence upper limit on GW background energy density, $\Omega_{GW}(25\text{ Hz}) \leq 2.0 \times 10^{-9}$ for a power-law GW background with a spectral index $\alpha = 2/3$ using data from the first part of LIGO, Virgo, and KAGRA's fourth observing run [68]. In our model presented in Sect. III, as we can see from Eq. (III.2,III.4), our prediction for Ω_{GW} also follows a power-law dependence on frequency $\propto f^{2/3}$ for BNS, BHNS, and BBH within the inspiral stage.

Model	$\Omega_{GW}^{tot}(65\text{ Hz})$	$\Omega_{GW}^{BNS}(65\text{ Hz})$	$\Omega_{GW}^{BBH}(65\text{ Hz})$	$\Omega_{GW}^{NSBH}(65\text{ Hz})$
Euclid	$1.73^{+1.67}_{-0.82} \times 10^{-10}$	$2.15^{+3.88}_{-1.71} \times 10^{-11}$	$1.25^{+0.78}_{-0.45} \times 10^{-10}$	$2.57^{+4.99}_{-1.93} \times 10^{-11}$
GWTC-3	$1.3^{+0.6}_{-0.4} \times 10^{-9}$	$1.1^{+3.2}_{-0.9} \times 10^{-10}$	$9.4^{+2.6}_{-3.4} \times 10^{-10}$	$1.7^{+4.2}_{-1.3} \times 10^{-10}$

TABLE I. Predicted total GW energy density for all three types of binaries (BNS, BBH, BHNS) with their highest 95% and lowest 5% confidence intervals from various methods. See text for details.

To assess the contributions to the total GW energy density across galaxies, Fig. 3 shows a 2D histogram of w_k^{GW} at 65 Hz as a function of the galaxy redshift, binned in 0.1-wide redshift bins. The left panel of Fig. 3 shows that most of the galaxies contributing to the total GW energy density have $w_k^{GW} \sim 10^{-22} - 10^{-20}$, with galaxies at the lowest redshifts can contribute as much as $w_k^{GW} \sim 10^{-16}$ (although these very loud galaxies are relatively rare). Summing over all galaxies in a given redshift bin, the right panel of Fig. 3 shows that most of the GW energy density comes from relatively low redshifts ($z \lesssim 1$), consistent with past work [e.g., 69]. This figure also shows that the sum of GW energy density at redshift $z = 3$ is about 15% of that at $z = 0.1$. Coupling with the absence of significant star-formation at higher redshifts, this result confirms that the redshift cut of $z < 3$ does not have a significant impact on our estimates.

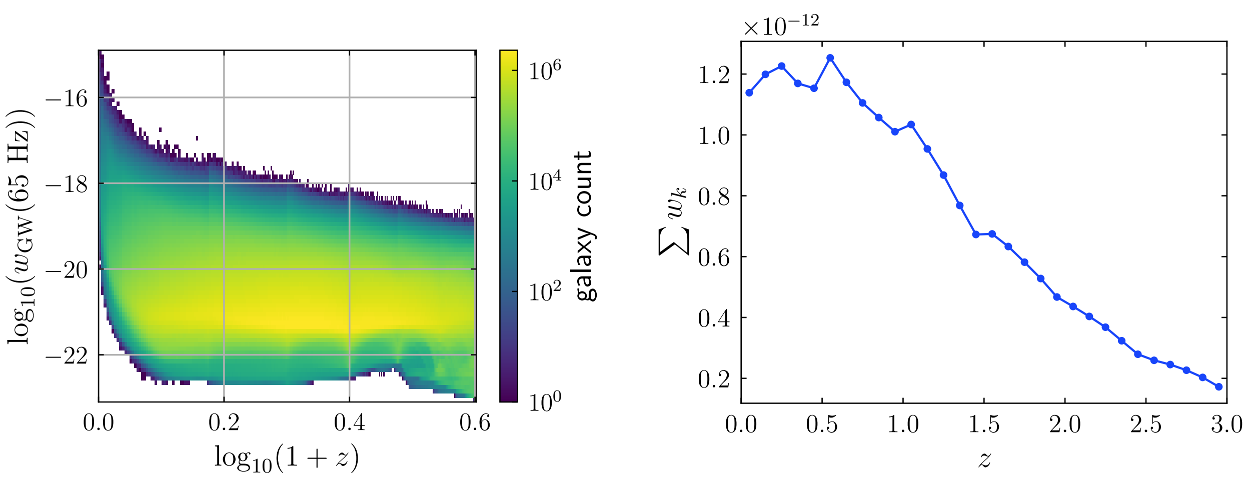

FIG. 3. *Left*: 2D binned histogram of $\log_{10} w_k^{GW}$ at 65 Hz and its $\log_{10}(1+z)$ for all *Euclid* galaxies. The colour bar shows number of galaxies in each bin. *Right*: sum of total GW energy density in 0.1-wide redshift bins from 0 to 3.

B. Gravitational-Wave Background Anisotropy

To study the anisotropy in our Catalogue-based model, we divide the sky into $N_{pix} = 786\,432$ pixels of 0.052 deg^2 each in `HEALPix` [70, 71] basis, equivalently $N_{side} = 256$. We choose such a high resolution to search for the small scale structure so as to compare it to the predictions of the astrophysical models in Sect. II. We then sum the GW energy density contributions from all galaxies in a given angular pixel p, normalizing it to the angular area of the pixel

$$\hat{\Omega}_p(f) = \frac{N_{\rm pix}}{4\pi} \sum_{k\in p} \sum_i w_{k,i}(f)\,. \tag{V.1}$$

Ω_p can then be used to display the GW energy density sky map using `HEALPix` [70, 71]. Since pixels at the edge of the sky region covered by the Catalogue are not fully populated by galaxies, these pixels (2023 out of 999 88 pixels) are removed from our analysis, as shown in Fig. 4. Consequently, the sky coverage fraction is modified to $1/f_{\rm sky} = 8.028$.

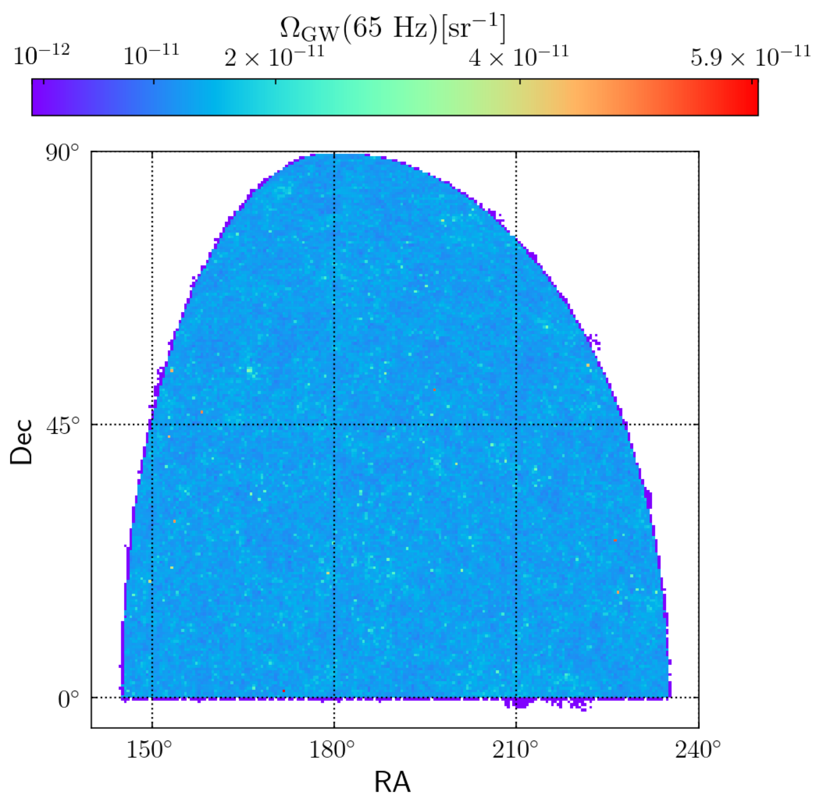

FIG. 4. Total GW energy density summed over all types of binaries (BNS, BBH, BHNS) at 65 Hz for all *Euclid* Flagship galaxies with $H_{\rm E}$ less than 26.6 per angular size in `HEALPix` for pixels of $N_{\rm pix} = 786\,432$ with removal of the edge pixels. The colours are on a log scale. The pixels in purple stand for the edge of the sky coverage, and are removed in all following calculation.

To compute the angular power spectra, we first define the pixel fluctuations in GW energy density relative to the average pixel energy density: $\delta\hat{\Omega}_p = \hat{\Omega}_p - \bar{\Omega}$. Here, the average pixel value $\bar{\Omega}$ is computed over the fully populated pixels covered by the *Euclid* Flagship Simulation Galaxy Catalogue. This pixelized sky map is then converted into a spherical harmonics decomposition, following [70]

$$\hat{a}_{\ell m} = \frac{4\pi}{N_{\rm pix}} \sum_{p=0}^{N_{\rm pix}-1} Y^*_{\ell m}(\mathbf{e}_p)\, \delta\hat{\Omega}_p\,, \tag{V.2}$$

where $\mathbf{e}_p$ is a unit vector pointing at the center of pixel p with sky location (θ, ϕ).

Following Sect. III and using the *Euclid* Flagship Simulation Galaxy Catalogue, we compute the expected GW background angular power spectrum due to compact binary mergers[2]. The angular power spectrum $\hat{C}_\ell^{\rm GW}$ is then estimated using the fluctuations as

$$\hat{C}_\ell^{\rm GW} = \frac{1}{(2\ell+1)\, f_{\rm sky}} \sum_{m=-\ell}^{\ell} \left|\hat{a}_{\ell m}\right|^2 , \tag{V.3}$$

with the corresponding cosmic variance being

$$\sigma_{\rm C}^2(\hat{C}_\ell^{\rm GW}) = \frac{2\,(\hat{C}_\ell^{\rm GW})^2}{(2\ell+1)\, f_{\rm sky}} . \tag{V.4}$$

Another source of variance comes from the uncertainty in the local merger rate in Eq. (III.9). This contribution $\sigma_{\rm R}^2(\hat{C}_\ell^{\rm GW})$ is estimated from the variations in $\hat{C}_\ell^{\rm GW}$ obtained by varying the merger rates of different types of binaries (BNS, BBH, BHNS) under the assumption of a Gaussian distribution. The total variance is then given by the two variances added quadratically

$$\sigma_{\rm tot}^2(\hat{C}_\ell^{\rm GW}) = \sigma_{\rm C}^2(\hat{C}_\ell^{\rm GW}) + \sigma_{\rm R}^2(\hat{C}_\ell^{\rm GW}) . \tag{V.5}$$

The result is shown in Fig. 5, including the uncertainty due to cosmic variance and due to the uncertainty in the local merger rates given in Eq. (III.9). We can see from this figure that the total variance $\sigma_{\rm tot}^2$ is dominated by the uncertainty of the local merger rate $\sigma_{\rm R}^2$ at high ℓ, but for $\ell < 20$, it is dominated by cosmic variance $\sigma_{\rm C}^2$, and its lower bound lies below the visible range on the logarithmic scale. This is because the partial sky coverage correction $f_{\rm sky}$ appears in the definition of cosmic variance in Eq. (V.4), implying that cosmic variance is of similar magnitude to $(\hat{C}_\ell^{\rm GW})^2$ at low ℓ. The figure also reveals oscillatory features in the $\hat{C}_\ell^{\rm GW}$ as a function of ℓ, primarily resulting from the fact that our sky coverage (roughly one octant of the sky) cannot provide information on large angular scales (low multipoles). To mitigate these fluctuations at higher ℓ, the curve can be smoothed by averaging over adjacent multipole bins rather than evaluating each integer ℓ individually.

Our predicted C_ℓ are $\sim 10^{10}$ below the latest broadband (20–1000 Hz) LIGO O3 *upper limits* on C_ℓ [72], which are derived assuming a power-law index $\alpha = 2/3$. We also compare with the narrow-band (60–70 Hz) LIGO upper limit of $\hat{C}_\ell^{\rm GW}$ reported in Fig. 4 of [16] ($\hat{C}_\ell^{\rm GW} \sim 10^{-14}$ at $\ell_{\rm max} = 5$). Similarly to C_ℓ, the current upper limits are well above the predicted signal, due to the limited sensitivity of the LIGO O3 campaign.

We note that estimates of the GW angular power spectra may be shot-noise-limited if the number of available galaxies in the catalogue is small. To illustrate this effect, we focus on the redshift bin $0 < z < 0.1$, in which the *Euclid* Flagship Simulation Galaxy Catalogue contains about 8.5 million galaxies (out of 4.8 billion in the entire Catalogue). The galaxies are split into 786 432 `HEALPix` sky map pixels of size 0.052 deg^2. We then apply the procedure developed in Sect. III to compute the SGWB angular power spectrum $\hat{C}_\ell^{\rm GW}$ defined in Eq. (V.3), which is shown as the blue solid curve in Fig. 6. We then randomly sample 15%, 20%, 30% of galaxies in each `HEALPix` pixel, and repeat this calculation. As galaxy count in pixels must be integers, the above choices of percentages ensure that every valid pixel is included during sampling (i.e., sample number in pixel ≥ 1), so we are using the same pixels without sampling for all the choices of samples. For every choice of samples, we replace the average of the GW energy density of all galaxies in every pixel

[2] Again, we note that no observational effects specific to *Euclid* are included in this calculation.

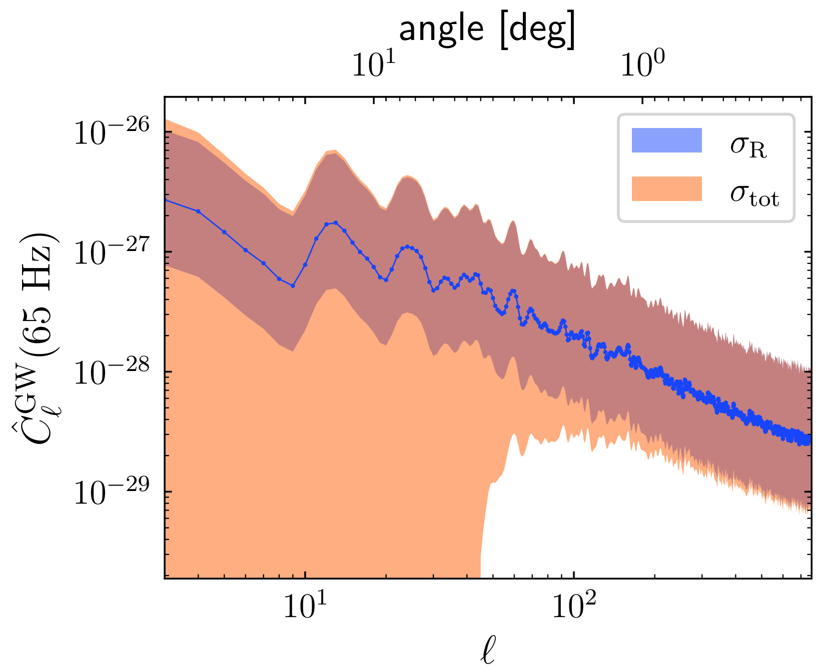

FIG. 5. GW energy density fluctuation C_ℓ defined in Eq. (V.3) is shown as a solid line, including contributions from all three binary types (BBH, BNS, and BHNS). Two 90% confidence uncertainty regions are shown: the blue region shows the uncertainty due to the uncertainty in the local merger rate, while the orange region shows the total uncertainty in Eq. (V.5).

by the average of the sampled galaxies. The resulting $\hat{C}_\ell^{GW}$ is shown in Fig. 6. As we can see in Fig. 6, when computed with fewer galaxies, $\hat{C}_\ell^{GW}$ plateaus at high values of ℓ as compared to the no-sampling case when all galaxies are used, and the plateau starts at lower ℓ as the sample size decreases. Hence, care must be taken when computing the angular power spectra to avoid possible bias due to shot noise limitations. Please note that the $\hat{C}_\ell^{GW}$ with 15% sampling is at lower level at $\ell \geq 10^2$ compared to 20% sampling, this is possibly due to the loss of energy with an incomplete catalogue. Nevertheless, this does not affect the trend that larger size of samples plateaus at higher values of ℓ, as the 20% sampling curve plateaus at higher values of ℓ compared to the 15% sampling curve. We note that Fig. 4 of [47] exhibits similar behavior – since this study was done using the *Millennium* simulation with about 5.7 million galaxies, we speculate that high-ℓ limit of their catalogue-based approach may have been impacted by the shot noise limitation.

C. Cross-Correlating GW Background and Galaxy Distribution

We next compute the angular power spectrum for cross-correlation between the GW background and the galaxy count distribution in the *Euclid* Flagship Simulation Galaxy Catalogue. As discussed above, this angular spectrum can be used as another astrophysical and cosmological probe [14].

The spherical harmonic decomposition of the GW background is discussed in Sect. V B. Regarding the galaxy counts, we define $\hat{n}_p$ as the number of Catalogue galaxies in the sky pixel p, and then compute the fluctuations in the galaxy number as $\hat{\Delta}_p = (\hat{n}_p - \bar{n})/\bar{n}$, where $\bar{n}$ is the average

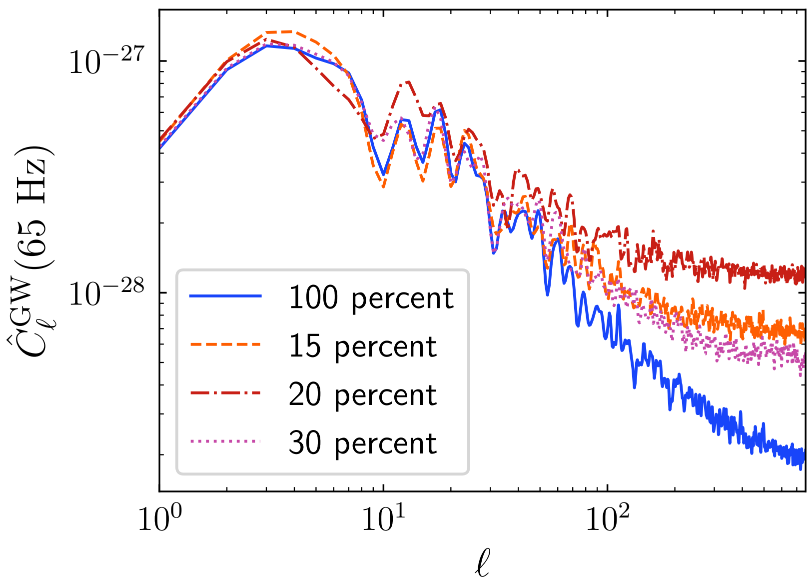

FIG. 6. GW angular power spectra at 65 Hz using all (100%) or 15%, 20%, 30% of galaxies with $0 < z < 0.1$ in the *Euclid* Flagship Simulation Galaxy Catalogue. The angular spectra computed with fewer galaxies plateau at high values of ℓ, and the plateau starts at lower values of ℓ if there are fewer galaxies in the sample.

number of galaxies per pixel. The spherical harmonic decomposition is then defined as

$$\hat{b}_{\ell m} = \frac{4\pi}{N_{\rm pix}} \sum_{p=0}^{N_{\rm pix}-1} Y^*_{\ell m}(\mathbf{e}_p)\, \hat{\Delta}_p\,. \tag{V.6}$$

The cross-correlation angular power spectrum is then computed as

$$\hat{C}_\ell^{\text{GW-gal}} = \frac{1}{(2\ell+1)\, f_{\rm sky}} \sum_{m=-\ell}^{\ell} \hat{b}^*_{\ell m}\, \hat{a}_{\ell m}\,, \tag{V.7}$$

We note that $\hat{a}_{\ell m}$ is computed using Eq. (V.2). The corresponding cosmic variance is [73]

$$\sigma^2_{\rm C}(\hat{C}_\ell^{\text{GW-gal}}) = \frac{\hat{C}_\ell^{\text{GW-GW}}\, \hat{C}_\ell^{\text{gal-gal}} + (\hat{C}_\ell^{\text{GW-gal}})^2}{(2\ell+1)\, f_{\rm sky}}\,. \tag{V.8}$$

Similarly to the auto-correlation case, the variance due to the local merger rate uncertainty, $\sigma^2_{\rm R}(\hat{C}_\ell^{\text{GW-gal}})$, is estimated from the variations in $\hat{C}_\ell^{\text{GW}-\text{gal}}$ obtained by varying the merger rates of different types of binaries (BNS, BBH, BHNS) under the assumption of a Gaussian distribution. The total variance is then

$$\sigma^2_{\rm tot}(\hat{C}_\ell^{\text{GW-gal}}) = \sigma^2_{\rm C}(\hat{C}_\ell^{\text{GW-gal}}) + \sigma^2_{\rm R}(\hat{C}_\ell^{\text{GW-gal}})\,. \tag{V.9}$$

Figure 7 shows the results of this calculation applied to the *Euclid* Flagship Simulation Galaxy Catalogue data. It also depicts the uncertainty due to the uncertainty in the local merger rates (Eq. III.9) and due to the total variance (Eq. V.9). Similar to the SGWB auto-correlation case in Figure

5, for $\ell < 40$ the total variance $\sigma^2_{\rm tot}(\hat{C}_\ell^{\rm cross})$ is dominated by cosmic variance of similar magnitude of $\hat{C}_\ell^{\rm cross}$ and its lower bound falls below the display threshold on a logarithmic scale due to partial sky coverage. The wiggling trend over ℓ is analogous to that in the SGWB auto-correlation case (see Figure 5).

Below, we will compare this simulation-based prediction with the semi-analytic astrophysical models discussed in Sect. II. The best-fit semi-analytic model is also shown in Figure 7, showing good agreement with our result for $\ell \geq 40$. At lower multipoles, the trend is not captured, but this is likely due to the partial sky coverage of the simulations, reflected in the large uncertainties at $\ell < 40$. The current upper limit on $\hat{C}_\ell^{\rm GW\text{-}gal}$ set by the LIGO O3 data in the 60–70 Hz frequency band is $\approx 10^{-9}$ for $\ell_{\rm max} = 5$ [Fig. 7 of [16]]. This value is about 10^7 times larger than the predicted signal, as expected by the limited sensitivity of the O3 LIGO data [74].

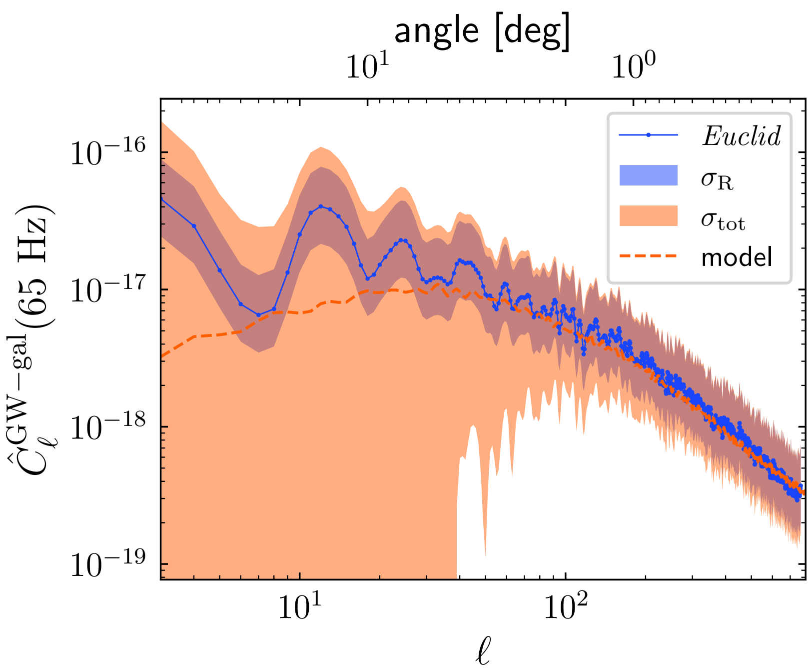

FIG. 7. Angular spectrum for cross-correlation between GW background and galaxy over-density is shown as a solid blue line. Two 90% confidence uncertainty regions are also shown including the uncertainty due to the local binary merger rate (blue) and due to the total variance (orange). For comparison, we show the red dashed line which is the astrophysical model $C_\ell^{\rm cross}(\theta)$ in Eq. (II.8) with the parameters θ being $A_0 = 1.42 \times 10^{-37} {\rm erg\,cm^{-3}\,s^{-1/3}}$, $z_c = 1.08$, $\sigma_z = 0.27$.

We proceed to relate this Catalogue-based estimate with the semi-analytic model discussed in Sect. II. The semi-analytic model depends on the astrophysical kernel $\mathcal{A}(f, z)$ and the window function $W(z)$. The window function is a flat window with an observational redshift limit cut, which in our case is $z = 3$.

In [14] different astrophysical models from binary compact objects formation and evolution have been explored. Each model was derived from a reference model by varying one key aspect, while keeping the others fixed, and adjusting an efficiency factor such that all of the models result in the same total number of detectable events. This exploratory approach identified a set of parameters as key in determining the angular power spectrum of the anisotropies. In particular, common features in the redshift dependence of the kernel (to the first approximation) can be captured by the following Gaussian parameterization

$$\mathcal{A}(f, z) = \mathcal{A}(f)\, \mathrm{e}^{-(z-z_c)^2/2\sigma_z^2} = A_0\, f^{-1/3}\, \mathrm{e}^{-(z-z_c)^2/2\sigma_z^2}\,, \tag{V.10}$$

where we used $z = z(r)$ to express the astrophysical kernel as a function of redshift and frequency. This parametrization of the kernel includes three free parameters in total $\theta = (A_0,\, z_c,\, \sigma_z)$: kernel amplitude A_0, peak redshift z_c, and peak width σ_z. For the set of models of [14] the range of parameters of the Gaussian fit for $0 < z < 2$ at 63 Hz are: $A_0 \in [1, 3] \times 10^{-37}\mathrm{erg\,cm^{-3}\,s^{-1/3}}$, $z_c \in [0.3, 1.8]$, $\sigma_z \in [0.3, 1.2]$.

To explore this parameter space in comparison with our Catalogue-based results, we define the logarithmic likelihood following the approach of [16]. To simplify the notation, we omit the subscript "GW-gal", understanding that all power spectra are the ones of the cross-correlation. We denote the angular power spectrum predicted from the Catalogue as $\hat{C}_\ell$, and we consider a perfect experiment where the covariance matrix is diagonal and given by the total variance as in Eq. (V.9). Since the covariance is diagonal, the logarithmic likelihood can be rewritten as

$$\ln \mathcal{L} = -\frac{1}{2} \ln |K_C| - \frac{1}{2}(C_\ell^t - \hat{C}_\ell)^T\, K_C^{-1}\, (C_\ell^t - \hat{C}_\ell) = -\frac{1}{2} \sum_\ell \left[\ln \sigma^2(\hat{C}_\ell) + \frac{(C_\ell^t - \hat{C}_\ell)^2}{\sigma^2(\hat{C}_\ell)} \right], \tag{V.11}$$

where the C_ℓ^t is the theoretical angular power spectrum of the cross-correlation [14, 16], dependent on the three parameters $(A_0,\, z_c,\, \sigma_z)$ of the Gaussian astrophysical kernel.

We then scan the 3-dimensional parameter space $(A_0,\, z_c,\, \sigma_z)$ with uniform priors of all three parameters with $A_0 \in [1 \times 10^{-38}, 5 \times 10^{-37}]\,\mathrm{erg\,cm^{-3}\,s^{-1/3}}$, $z_c \in [0.20, 1.80]$, $\sigma_z \in [0.01, 1.20]$. The resulting posterior probability curves and contour plots are presented in Fig. 8. The best-fit parameters are $A_0 = 1.4 \times 10^{-37}\mathrm{erg\,cm^{-3}\,s^{-1/3}}$, $z_c = 1.08$, $\sigma_z = 0.27$. These results have to be understood as best-fit parameters for a perfect experiment observing the *Euclid* Flagship Simulation Galaxy Catalogue of galaxies, with zero instrumental noise and cosmic-variance limited. The model $C_\ell^{\mathrm{t}}(\theta)$ with the best-fit parameters are also shown in Fig. 7 in red dashed line, we can see that it matches our cross-correlation estimator $\hat{C}_\ell^{\mathrm{GW-gal}}$ for ℓ larger than 40. We observe that the best-fit value for the amplitude A_0 lies within the range of values spanned by the astrophysical models explored in [14].

VI. DISCUSSION AND CONCLUSION

The origin of compact binaries remains uncertain and is a subject of extensive debate. Broadly, two primary formation channels can be identified: the isolated channel, where compact binaries emerge as a byproduct of binary stellar evolution, and the dynamical channel, in which compact binaries—or their progenitors—form through gravitational interactions in dense stellar environments. These differing formation processes are expected to be reflected in the source distribution and hence in the SGWB spectrum.

Cross-correlation techniques can provide valuable insights into the formation channels of binary systems. Firstly, they enable tomographic redshift reconstruction. Furthermore, by selecting specific subpopulations from a catalogue of galaxies, this method can help identify which groups are responsible for the majority of gravitational wave emissions.

In this paper, we estimated the amplitude and spatial anisotropy in the SGWB energy density due to compact binary coalescence events, making use of the *Euclid* Flagship Simulation Galaxy

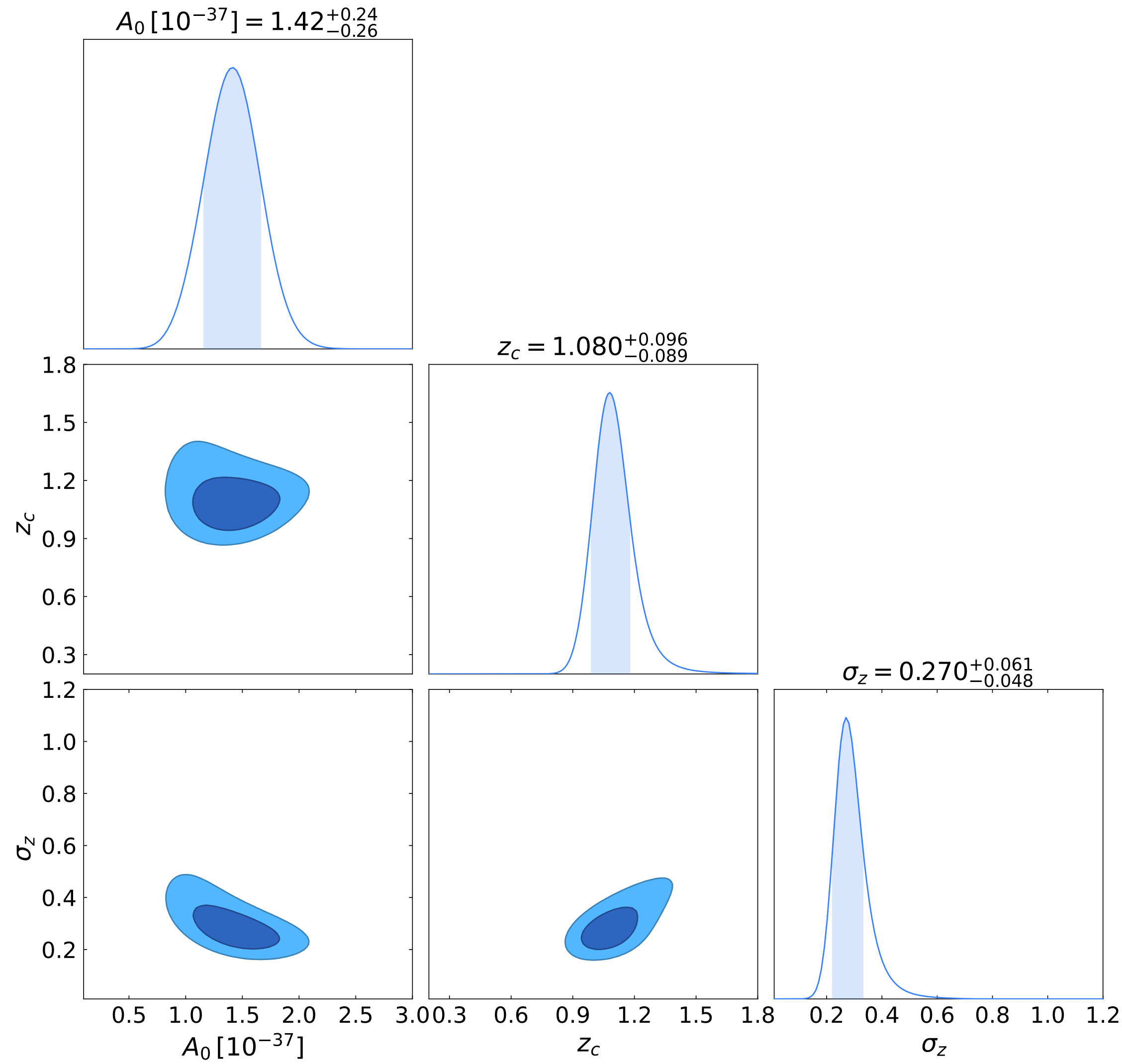

FIG. 8. Contour plots using ChainConsumer [75] in 3D parameter space of (A_0, z_c, σ_z) for GW fluctuation $\times$ galaxy over-density cross-correlation $\hat{C}_\ell$ and astrophysical model $C_\ell(\theta)$, $\theta = (A_0, z_c, \sigma_z)$ with uniform priors for all parameters.

Catalogue (version 2.1.10) [25]. We implemented an SFH model $\psi(z)$ for each galaxy, driven by its current star-formation rate and total stellar mass specified in the Catalogue. We combined the SFH model with a distribution of time delay $p(t_\mathrm{d})$ between binary formation and merger, and with the distribution of metallicity $p(\mathcal{Z})$ to obtain the merger rate of compact binaries hosted by the galaxies. We then used the latest estimates of the mass distribution for compact binaries, provided by Advanced LIGO and Advanced Virgo observations through GWTC-3 [46], and followed the method of [45] to compute the SGWB energy density due to the entire population of merging compact binaries. Using this method, we predicted both the angular power spectrum of the resulting SGWB anisotropy and its cross-correlation with the galaxy distribution.

Finally, we compared our predictions with previous results in the literature obtained by using the *Millennium* simulation, and to predictions of semi-analytic models such as the ones of [14]. After direct inspection, we find that the astrophysical dependence can be effectively parametrised introducing a Gaussian kernel, dependent on three parameters. Assuming a perfect experiment with zero instrumental noise, we applied a Bayesian approach to explore the parameter space of this kernel and set constraints on the model parameters. The resulting best-fit values are within the realistic range of values predicted in the explorative approach of [14].

This exercise serves as an initial step toward developing a consistent framework for utilizing future *Euclid* data. We showed that future measurements of the SGWB angular power spectrum and the SGWB-galaxy correlation angular power spectrum can be used to constrain the combination of ψ, $p(t_{\rm d})$, and $p(\mathcal{Z})$. Moreover, combining these measurements with other observations (e.g. SFH measurements by *Euclid*) can then further constrain the remaining quantities. The next step will involve incorporating simulated noise components into the *Euclid* Flagship Simulation Galaxy Catalogue, and replicating realistic LVK background noise. This preparation will enhance our ability to analyze both galaxy and background data, allowing us to anticipate the expected outcomes of future correlations.

ACKNOWLEDGMENTS

This work has made use of CosmoHub, developed by PIC (maintained by IFAE and CIEMAT) in collaboration with ICE-CSIC. CosmoHub received funding from the Spanish government (MCIN/AEI/10.13039/501100011033), the EU NextGeneration/PRTR (PRTR-C17.I1), and the Generalitat de Catalunya.

The authors are grateful for computational resources provided by the LIGO Laboratory (CIT) supported by National Science Foundation Grants PHY-0757058 and PHY-0823459 and Inter-University Center for Astronomy and Astrophysics (Sarathi).

The work of KY, CS, and VM was in part supported by NSF grants PHY-2308486 and PHY-2011675.

The Euclid Consortium acknowledges the European Space Agency and a number of agencies and institutes that have supported the development of *Euclid*, in particular the Agenzia Spaziale Italiana, the Austrian Forschungsförderungsgesellschaft funded through BMIMI, the Belgian Science Policy, the Canadian Euclid Consortium, the Deutsches Zentrum für Luft- und Raumfahrt, the DTU Space and the Niels Bohr Institute in Denmark, the French Centre National d'Etudes Spatiales, the Fundação para a Ciência e a Tecnologia, the Hungarian Academy of Sciences, the Ministerio de Ciencia, Innovación y Universidades, the National Aeronautics and Space Administration, the National Astronomical Observatory of Japan, the Netherlandse Onderzoekschool Voor Astronomie, the Norwegian Space Agency, the Research Council of Finland, the Romanian Space Agency, the State Secretariat for Education, Research, and Innovation (SERI) at the Swiss Space Office (SSO), and the United Kingdom Space Agency. A complete and detailed list is available on the *Euclid* web site (`www.euclid-ec.org`).

---

[1] LIGO Scientific Collaboration. Advanced LIGO. *Classical and Quantum Gravity*, 32(7):074001, April 2015.

[2] F. Acernese, M. Agathos, and K. Agatsuma et al. Advanced Virgo: a second-generation interferometric gravitational wave detector. *Classical and Quantum Gravity*, 32(2):024001, January 2015.

[3] T. Akutsu, M. Ando, and K. Arai et al. Overview of KAGRA: Calibration, detector characterization, physical environmental monitors, and the geophysics interferometer. *Progress of Theoretical and Experimental Physics*, 2021(5):05A102, May 2021.

[4] The LIGO Scientific Collaboration, the Virgo Collaboration, and the KAGRA Collaboration. GWTC-4.0: Updating the Gravitational-Wave Transient Catalog with Observations from the First Part of the Fourth LIGO-Virgo-KAGRA Observing Run. arXiv:2508.18082, August 2025.

[5] The LIGO Scientific Collaboration, the Virgo Collaboration, and the KAGRA Collaboration. Gwtc-4.0: Population properties of merging compact binaries. arXiv:2508.18083, August 2025.

[6] The LIGO Scientific Collaboration, the Virgo Collaboration, and the KAGRA Collaboration. Tests of General Relativity with GWTC-3. arXiv:2112.06861, December 2021.

[7] The LIGO Scientific Collaboration, the Virgo Collaboration, and the KAGRA Collaboration. Gwtc-4.0: Constraints on the cosmic expansion rate and modified gravitational-wave propagation. arXiv:2509.04348, September 2025.

[8] B. P. Abbott, R. Abbott, and T. D. Abbott et al. GW170817: Measurements of neutron star radii and equation of state. *Phys. Rev. Lett.*, 121(16):161101, October 2018.

[9] M. Maggiore. Gravitational wave experiments and early universe cosmology. *Physics Reports*, 331(6):283–367, July 2000.

[10] T. Regimbau. The astrophysical gravitational wave stochastic background. *Res. Astron. Astrophys.*, 11(4):369–390, March 2011.

[11] A. C. Jenkins and M. Sakellariadou. Shot noise in the astrophysical gravitational-wave background. *Phys. Rev.*, D100(6):063508, September 2019.

[12] A. C. Jenkins, J. D. Romano, , and M. Sakellariadou. Estimating the angular power spectrum of the gravitational-wave background in the presence of shot noise. *Phys. Rev.*, D100(8):083501, October 2019.

[13] D. Alonso, G. Cusin, and P. G. Ferreira et al. Detecting the anisotropic astrophysical gravitational wave background in the presence of shot noise through cross-correlations. *Phys. Rev. D*, 102(2):023002, July 2020.

[14] G. Cusin, I. Dvorkin, and C. Pitrou et al. Properties of the stochastic astrophysical gravitational wave background: astrophysical sources dependencies. *Phys. Rev. D*, 100(6):063004, September 2019.

[15] K. Z. Yang, V. Mandic, and C. Scarlata et al. Searching for Cross-Correlation Between Stochastic Gravitational Wave Background and Galaxy Number Counts. *MNRAS*, 500(2):1666–1672, January 2021.

[16] K. Z. Yang, J. Suresh, and G. Cusin et al. Measurement of the cross-correlation angular power spectrum between the stochastic gravitational wave background and galaxy overdensity. *Phys. Rev. D*, 108(4):043025, August 2023.

[17] G. Cusin, I. Dvorkin, and C. Pitrou et al. First predictions of the angular power spectrum of the astrophysical gravitational wave background. *Phys. Rev. Lett.*, 120(23):231101, June 2018.

[18] G. Capurri, A. Lapi, and C. Baccigalupi et al. Intensity and anisotropies of the stochastic gravitational wave background from merging compact binaries in galaxies. *JCAP*, 11:032, November 2021.

[19] D. Alonso, M. Nikjoo, and A. I. Renzini et al. Tomographic constraints on the production rate of gravitational waves from astrophysical sources. *Phys. Rev. D*, 110(10):103544, November 2024.

[20] M. R. Sah and S. Mukherjee. Non-stationary astrophysical stochastic gravitational-wave background: a new probe to the high-redshift population of binary black holes. *MNRAS*, 527(2):4100–4111, January 2024.

[21] S. Mukherjee and J. Silk. Time-dependence of the astrophysical stochastic gravitational wave background. *MNRAS*, 491(4):4690–4701, November 2020.

[22] S. Ferraiuolo, S. Mastrogiovanni, and S. Escoffier et al. Inferring astrophysics and cosmology with individual compact binary coalescences and their gravitational-wave stochastic background. *A&A*, 701:A36, September 2025.

[23] G. Cusin, C. Pitrou, and M. Pijnenburg et al. Measuring anisotropies in the PTA band with cross-correlations. arXiv:2502.17401, February 2025.

[24] C. Pitrou and G. Cusin. Mitigating cosmic variance in the Hellings-Downs curve: A cosmic microwave background analogy. *Phys. Rev. D*, 111(8):083544, April 2025.

[25] Euclid Collaboration: F. J. Castander, P. Fosalba, and J. Stadel et al. Euclid: V. The Flagship galaxy mock catalogue: A comprehensive simulation for the Euclid mission. *A&A*, 697:A5, May 2025.

[26] L. P. Grishchuk. Amplification of gravitational waves in an isotropic universe. *Soviet Journal of Experimental and Theoretical Physics*, 40:409, September 1975.

[27] R. Bar-Kana. Limits on direct detection of gravitational waves. *Phys. Rev. D*, 50(2):1157–1160, July 1994.

[28] A. A. Starobinskiǐ. Spectrum of relict gravitational radiation and the early state of the universe. *Soviet Journal of Experimental and Theoretical Physics Letters*, 30:682, December 1979.

[29] M. S. Turner. Detectability of inflation produced gravitational waves. *Phys. Rev. D*, 55(2):R435–R439, January 1997.

[30] N. Barnaby, E. Pajer, and M. Peloso. Gauge field production in axion inflation: Consequences for monodromy, non-Gaussianity in the CMB, and gravitational waves at interferometers. *Phys. Rev. D*, 85(2):023525, January 2012.

[31] N. Seto and A. Taruya. Measuring a Parity-Violation Signature in the Early Universe via Ground-Based Laser Interferometers. *Phys. Rev. Lett.*, 99(12):121101, September 2007.

[32] R. Easther and E. A. Lim. Stochastic gravitational wave production after inflation. *JCAP*, 2006(4):010, April 2006.

[33] R. R. Caldwell and B. Allen. Cosmological constraints on cosmic string gravitational radiation. *Phys. Rev. D*, 45(10):3447–3468, May 1992.

[34] T. Damour and A. Vilenkin. Gravitational Wave Bursts from Cosmic Strings. *Phys. Rev. Lett.*, 85(18):3761–3764, October 2000.

[35] T. Damour and A. Vilenkin. Gravitational radiation from cosmic (super)strings: Bursts, stochastic background, and observational windows. *Phys. Rev. D*, 71(6):063510, March 2005.

[36] X. Siemens, V. Mandic, and J. Creighton. Gravitational-Wave Stochastic Background from Cosmic Strings. *Phys. Rev. Lett.*, 98(11):111101, March 2007.

[37] T. Regimbau and J. A. de Freitas Pacheco. Stochastic background from coalescences of neutron star–neutron star binaries. *ApJ*, 642(1):455–461, May 2006.

[38] X.-J. Zhu, E. Howell, and T. Regimbau et al. Stochastic gravitational wave background from coalescing binary black holes. *ApJ*, 739(2):86, October 2011.

[39] S. Marassi, R. Schneider, and G. Corvino et al. Imprint of the merger and ring-down on the gravitational wave background from black hole binaries coalescence. *Phys. Rev. D*, 84(12):124037, December 2011.

[40] C. Cutler. Gravitational waves from neutron stars with large toroidal *b* fields. *Phys. Rev. D*, 66(8):084025, October 2002.

[41] S. Bonazzola and E. Gourgoulhon. Gravitational waves from pulsars: emission by the magnetic field induced distortion. *A&A*, 312:675–690, August 1996.

[42] S. Marassi, R. Ciolfi, and R. Schneider et al. Stochastic background of gravitational waves emitted by magnetars. *MNRAS*, 411(4):2549–2557, March 2011.

[43] D. M. Coward, R. R. Burman, and D. G. Blair. Simulating a stochastic background of gravitational waves from neutron star formation at cosmological distances. *MNRAS*, 329(2):411–416, January 2002.

[44] G. Cusin, I. Dvorkin, and C. Pitrou et al. Stochastic gravitational wave background anisotropies in the mHz band: astrophysical dependencies. *MNRAS*, 493(1):L1–L5, March 2020.

[45] A. C. Jenkins, R. O'Shaughnessy, and M. Sakellariadou et al. Anisotropies in the astrophysical gravitational-wave background: The impact of black hole distributions. *Phys. Rev. Lett.*, 122(11):111101, March 2019.

[46] R. Abbott, T. D. Abbott, and F. Acernese et al. Population of Merging Compact Binaries Inferred Using Gravitational Waves through GWTC-3. *Phys. Rev. X*, 13(1):011048, January 2023.

[47] A. C. Jenkins, M. Sakellariadou, and T. Regimbau et al. Anisotropies in the astrophysical gravitational-wave background: Predictions for the detection of compact binaries by LIGO and Virgo. *Phys. Rev.*, D98(6):063501, September 2018.

[48] G. Cusin, C. Pitrou, and J.-P. Uzan. Anisotropy of the astrophysical gravitational wave background: Analytic expression of the angular power spectrum and correlation with cosmological observations. *Phys. Rev. D*, 96(10):103019, November 2017.

[49] G. Cusin, C. Pitrou, and J.-P. Uzan. The signal of the gravitational wave background and the angular correlation of its energy density. *Phys. Rev. D*, 97(12):123527, June 2018.

[50] C. Pitrou, G. Cusin, and J. P. Uzan. Unified view of anisotropies in the astrophysical gravitational-wave background. *Phys. Rev. D*, 101(8):081301, April 2020.

[51] G. Cusin, R. Durrer, and P. G. Ferreira. Polarization of a stochastic gravitational wave background through diffusion by massive structures. *Phys. Rev. D*, 99(2):023534, January 2019.

[52] F. A. Marin, C. Blake, and G. B. Poole et al. The WiggleZ Dark Energy Survey: constraining galaxy bias and cosmic growth with 3-point correlation functions. *MNRAS*, 432(4):2654–2668, July 2013.

[53] A. Rassat, A. Amara, and L. Amendola et al. Deconstructing Baryon Acoustic Oscillations: A Comparison of Methods. arXiv:0810.0003, October 2008.

[54] G. Cusin, C. Pitrou, and C. Bonvin et al. Boosting gravitational waves: a review of kinematic effects on amplitude, polarization, frequency and energy density. *Class. Quant. Grav.*, 41(22):225006, October 2024.

[55] P. Ajith, M. Hannam, and S. Husa et al. Inspiral-merger-ringdown waveforms for black-hole binaries with nonprecessing spins. *Phys. Rev. Lett.*, 106(24):241101, June 2011.

[56] P. Tallada, J. Carretero, and J. Casals et al. CosmoHub: Interactive exploration and distribution of astronomical data on Hadoop. *Astron. Comput.*, 32:100391, July 2020.

[57] J. Carretero, P. Tallada, and J. Casals et al. CosmoHub and SciPIC: Massive cosmological data analysis, distribution and generation using a Big Data platform. *PoS*, EPS-HEP2017:488, July 2017.

[58] M. Curti, F. Mannucci, and G. Cresci et al. The mass-metallicity and the fundamental metallicity relation revisited on a fully T_e-based abundance scale for galaxies. *MNRAS*, 491(1):944–964, January 2020.

[59] C. Allende Prieto, D. L. Lambert, and M. Asplund. The forbidden abundance of oxygen in the sun. *ApJL*, 556(1):L63–L66, July 2001.

[60] A. Renzini. Stellar population diagnostics of elliptical galaxy formation. *ARA&A*, 44(1):141–192, September 2006.

[61] D. Thomas, C. Maraston, and R. Bender et al. The Epochs of Early-Type Galaxy Formation as a Function of Environment. *ApJ*, 621(2):673–694, March 2005.

[62] C. A. Mason, M. Trenti, and T. Treu. The galaxy uv luminosity function before the epoch of reionization. *ApJ*, 813(1):21, November 2015.

[63] E. Vangioni, K. A. Olive, and T. Prestegard et al. The impact of star formation and gamma-ray burst rates at high redshift on cosmic chemical evolution and reionization. *MNRAS*, 447(3):2575–2587, March 2015.

[64] P. Madau and M. Dickinson. Cosmic Star-Formation History. *ARA&A*, 52:415–486, August 2014.

[65] B. Diemer, M. Sparre, and L. E. Abramson et al. Log-normal star formation histories in simulated and

observed galaxies. *ApJ*, 839(1):26, April 2017.

[66] B. P. Abbott, R. Abbott, T. D. Abbott, et al. Gw170817: Implications for the stochastic gravitational-wave background from compact binary coalescences. *Phys. Rev. Lett.*, 120(9):091101, March 2018.

[67] B. P. Abbott, R. Abbott, T. D. Abbott, et al. Upper limits on the rates of binary neutron star and neutron star-black hole mergers from advanced ligo's first observing run. *ApJL*, 832(2):L21, December 2016.

[68] The LIGO Scientific Collaboration, the Virgo Collaboration, and the KAGRA Collaboration. Upper Limits on the Isotropic Gravitational-Wave Background from the first part of LIGO, Virgo, and KAGRA's fourth Observing Run. arXiv:2508.20721, August 2025.

[69] C. Wu, V. Mandic, and T. Regimbau. Accessibility of the gravitational-wave background due to binary coalescences to second and third generation gravitational-wave detectors. *Phys. Rev. D*, 85(10):104024, May 2012.

[70] A. Zonca, L. Singer, and D. Lenz et al. healpy: equal area pixelization and spherical harmonics transforms for data on the sphere in python. *Journal of Open Source Software*, 4(35):1298, March 2019.

[71] K. M. Górski, E. Hivon, and A. J. Banday et al. HEALPix: A Framework for High-Resolution Discretization and Fast Analysis of Data Distributed on the Sphere. *ApJ*, 622(2):759–771, April 2005.

[72] R. Abbott, T. D. Abbott, and S. Abraham et al. Search for anisotropic gravitational-wave backgrounds using data from Advanced LIGO and Advanced Virgo's first three observing runs. *Phys. Rev. D*, 104(2):022005, July 2021.

[73] T. Louis, X. Garrido, and A. Soussana et al. Consistency of CMB experiments beyond cosmic variance. *Phys. Rev. D*, 100(2):023518, July 2019.

[74] A. Buikema, C. Cahillane, G. L. Mansell, et al. Sensitivity and performance of the Advanced LIGO detectors in the third observing run. *Phys. Rev. D*, 102(6):062003, September 2020.

[75] S. R. Hinton. ChainConsumer. *The Journal of Open Source Software*, 1:00045, August 2016.